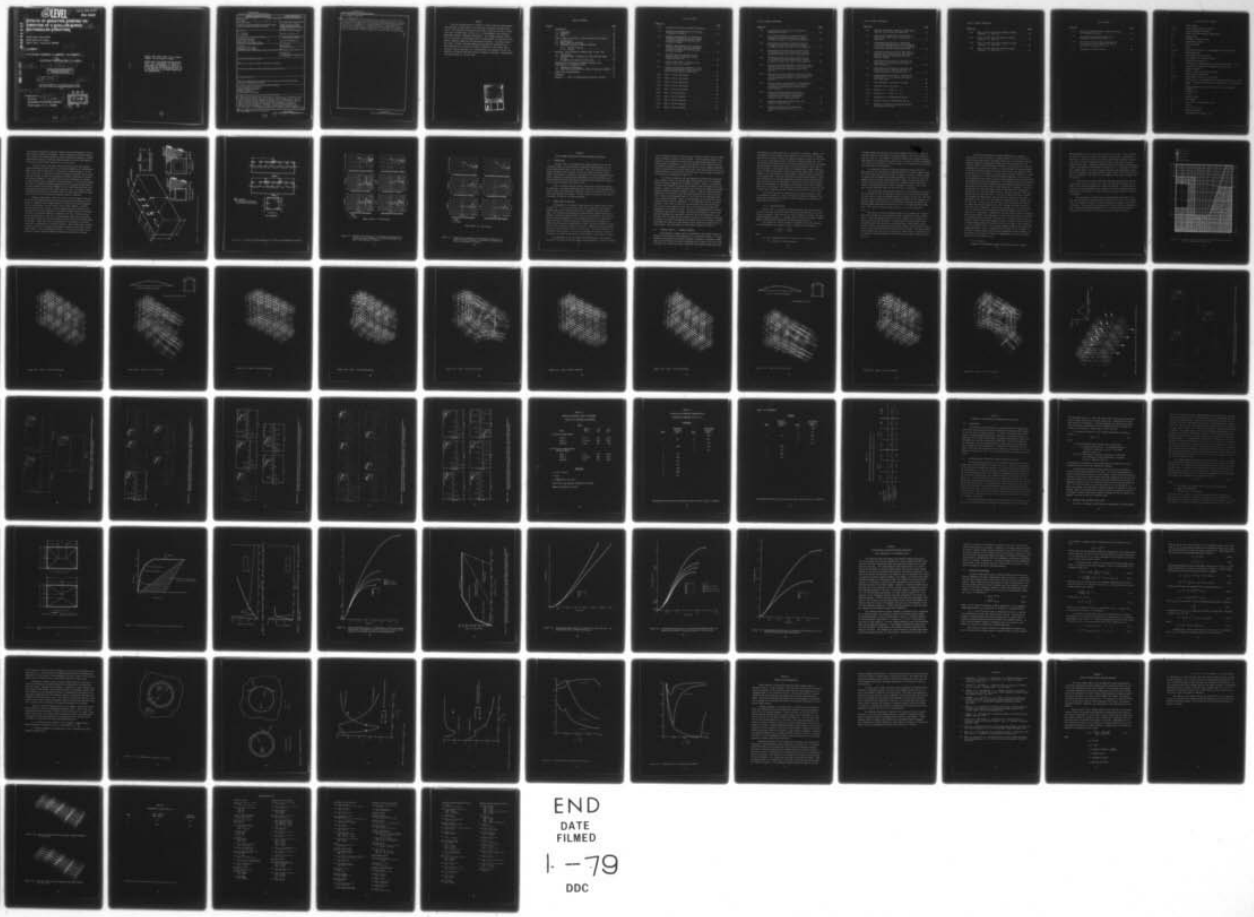
AD-A061 442 WEIDLINGER ASSOCIATES MENLO PARK CALIF F/G 13/13
EFFECTS OF RADIATION DAMPING ON VIBRATION OF A SHALLOW-BURIED R--ETC(U)
APR 78 G L WOJCIK, J ISENBERG DNA001-77-C-0233
UNCLASSIFIED R-7818 DNA-4600F NL

1 OF
AD
A061442



END
DATE
FILMED
1-79
DDC

AD A061442

DDC FILE COPY

(12) LEVEL II

AD-E300 370

DNA 4600F

(6)

EFFECTS OF RADIATION DAMPING ON VIBRATION OF A SHALLOW-BURIED RECTANGULAR STRUCTURE

Weidlinger Associates
3000 Sand Hill Road
Menlo Park, California 94025

(12) 90p.

(11) April 1978

(9) Final Report for Period August 1977—March 1978

(15) CONTRACT No. DNA 001-77-C-0233

(10) G. L. /Wojcik J. /Isenberg

APPROVED FOR PUBLIC RELEASE;
DISTRIBUTION UNLIMITED.

(14) R-7818

(17) C061

THIS WORK SPONSORED BY THE DEFENSE NUCLEAR AGENCY
UNDER RDT&E RMSS CODE B344077464 Y99QAXSC06152 H2590D.

(16)

(18) DNA, SBIE

Prepared for
Director
DEFENSE NUCLEAR AGENCY
Washington, D. C. 20305

(19) 4600 F,
AD-E300 370

DDC
RECEIVED
NOV 22 1978
B

JOB

392 150 78 10 05 038

Destroy this report when it is no longer needed. Do not return to sender.

PLEASE NOTIFY THE DEFENSE NUCLEAR AGENCY, ATTN: TISI, WASHINGTON, D.C. 20305, IF YOUR ADDRESS IS INCORRECT, IF YOU WISH TO BE DELETED FROM THE DISTRIBUTION LIST, OR IF THE ADDRESSEE IS NO LONGER EMPLOYED BY YOUR ORGANIZATION.

DNA PRINTING PLANT

UNCLASSIFIED

SECURITY CLASSIFICATION OF THIS PAGE *(When Data Entered)*

REPORT DOCUMENTATION PAGE		READ INSTRUCTIONS BEFORE COMPLETING FORM
1. REPORT NUMBER DNA 4600F	2. GOVT ACCESSION NO.	3. RECIPIENT'S CATALOG NUMBER
4. TITLE *(and Subtitle)* EFFECTS OF RADIATION DAMPING ON VIBRATION OF A SHALLOW-BURIED RECTANGULAR STRUCTURE		5. TYPE OF REPORT & PERIOD COVERED Final Report for Period August 1977-March 1978 6. PERFORMING ORG. REPORT NUMBER R 7818
7. AUTHOR(s) G. L. Wojcik J. Isenberg		8. CONTRACT OR GRANT NUMBER(s) DNA 001-77-C-0233
9. PERFORMING ORGANIZATION NAME AND ADDRESS Weidlinger Associates 3000 Sand Hill Road Menlo Park, California 94025		10. PROGRAM ELEMENT, PROJECT, TASK AREA & WORK UNIT NUMBERS Subtask Y99QAXSC061-52
11. CONTROLLING OFFICE NAME AND ADDRESS Director Defense Nuclear Agency Washington, D.C. 20305		12. REPORT DATE April 1978 13. NUMBER OF PAGES 88
14. MONITORING AGENCY NAME & ADDRESS*(if different from Controlling Office)*		15. SECURITY CLASS *(of this report)* UNCLASSIFIED 15a. DECLASSIFICATION/DOWNGRADING SCHEDULE

16. DISTRIBUTION STATEMENT *(of this Report)*

Approved for public release; distribution unlimited.

17. DISTRIBUTION STATEMENT *(of the abstract entered in Block 20, if different from Report)*

18. SUPPLEMENTARY NOTES

This work sponsored by the Defense Nuclear Agency under RDT&E RMSS Code B344077464 Y99QAXSC06152 H2590D.

19. KEY WORDS *(Continue on reverse side if necessary and identify by block number)*

Structure-Medium Interaction
Finite Element Simulation
Radiation Damping
Single-degree-of-freedom

20. ABSTRACT *(Continue on reverse side if necessary and identify by block number)*

Radiation damping from shallow-buried structures of rectangular cross-section was analyzed by means of an elastic, finite element model. The results show that radiation damping increases with the stiffness of backfill, which is consistent with results previously obtained for a buried arch. Implications are examined of including a viscous damping mechanism to simulate radiation damping in nonlinear single-degree-of-freedom models of the roof slab. In the examples considered, including radiation damping

DD FORM 1 JAN 73 1473 EDITION OF 1 NOV 65 IS OBSOLETE

UNCLASSIFIED

SECURITY CLASSIFICATION OF THIS PAGE *(When Data Entered)*

78 10 05 038

20. ABSTRACT (Continued)

up to 20% ~~percent~~ of critical (based on the stiffness of the slab in the elastic-cracked regime), reduces calculated peak displacements to as little as one-half of the magnitude as calculated by SDOF models without damping. To explain the dependence of radiation damping on deformational mode number, an exact analysis of a cylindrical elastic, plane strain section in an infinite elastic domain was performed. As expected, the findings indicate that higher radiation damping is associated with the lower modes.

SUMMARY

The work reported below is related to forced vibration testing which was performed on approximately one-third scale reinforced concrete structures. The tests were performed at Fort Polk, Louisiana, in 1975 in connection with the ESSEX Phase 3 Event by U. S. Army Engineer Corps Waterways Experiment Station, Vicksburg, Mississippi. The present analytic study is part of a series of calculations aimed at investigating the parameters which govern radiation damping in shallow-buried structures. A previous report, DNA 4281F, considers radiation damping associated with deformations of a shallow-buried arch for several backfill conditions. The present report considers similar phenomena for a shallow-buried rectangular structure and applies the findings regarding radiation damping to nonlinear, single-degree-of-freedom models of the roof slab.

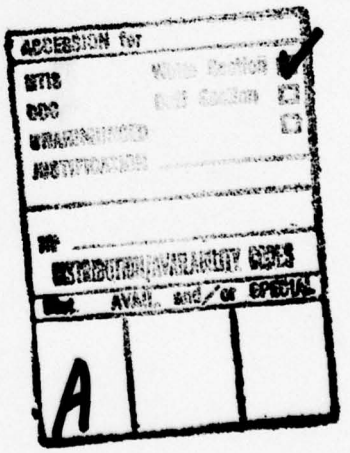


TABLE OF CONTENTS

Section		Page
1	INTRODUCTION	9
	1.1. BACKGROUND	9
	1.2. OBJECTIVE	10
	1.3. SCOPE	10
2	FINITE ELEMENT SIMULATION OF BURIED RECTANGULAR STRUCTURES	16
	2.1. INTRODUCTION	16
	2.2. NORMAL MODES OF STRUCTURE	16
	2.3. TRANSIENT ANALYSIS OF COVERED STRUCTURE	17
	2.3.1. Radiation Damping	18
	2.3.2. Arching	20
3	NONLINEAR, SINGLE-DEGREE-OF-FREEDOM MODEL OF ROOF SLAB	48
	3.1. INTRODUCTION	48
	3.2. EQUIVALENT MASS, STIFFNESS AND LOADS FOR SDOF MODEL OF SLAB	48
	3.3. NONLINEAR SDOF ANALYSES OF ROOF SLABS	49
4	SCALING RULES FOR RADIATION DAMPING ASSOCIATES WITH VIBRATIONS OF A CYLINDRICAL CAVITY	61
	4.1. THEORETICAL DEVELOPMENT	62
	4.2. SOLUTION AND APPLICATION TO CASES OF PRACTICAL INTEREST.	66
5	SUMMARY AND RECOMMENDATIONS	74
	REFERENCES	76
	APPENDIX I — STUDY OF DISCRETIZATION USED FOR STRUCTURE	77

LIST OF FIGURES

Figure No.		Page
1-1	Rectangular Structure and Backfill Geometry	12
1-2	Geometry and Instumentation for Arch and Rectangular Structures	13
1-3	Impedance and Quadrature for Rectangular Structures 3B Before and After Placement of Backfill Determined from Tests with Vibrators In Phase	14
1-4	Impedance and Quadrature for Rectangular Structure 3D Before and After Placement of Backfill Determined from Tests with Vibrators In Phase	15
2-1	Elevation View of Transverse Section Through Finite Element Model of Rectangular Structure 3D	22
2-2	Finite Element Model of Structure (for clarity, soil is not shown)	23
2-3	Uniaxial Stress-Strain Properties of Compacted Native Backfill (Arch) and Cook's Bayou Sand (Rectangular Structures)	24
2-4a.	Mode 1, 112 Hz (Uncovered)	25
2-4b	Mode 2, 214 Hz (Uncovered)	26
2-4c.	Mode 3, 235 Hz (Uncovered)	27
2-4d.	Mode 4, 333 Hz (Uncovered)	28
2-4e.	Mode 5, 353 Hz (Uncovered)	29
2-5a.	Mode 1, 88 Hz (Covered)	30
2-5b.	Mode 2, 172 Hz (Covered)	31
2-5c.	Mode 3, 180 Hz (Covered)	32
2-5d.	Mode 4, 271 Hz (Covered)	33
2-5e.	Mode 5, 293 Hz (Covered)	34

LIST OF FIGURES (CONTINUED)

Figure No.		Page
2-6	Loads Applied to Structure for Analyses of Transient Vibrations	35
2-7	Velocity-Time Histories at Various Points on Rectangular Structure Subjected to Loading as Shown in Figure 2-6, Case 1 (Soft Backfill)	36
2-8	Velocity-Time Histories at Various Points on Rectangular Structures Subjected to Loading as Shown in Figure 2-6, Case 2 (Stiff Backfill)	37
2-9	Displacement-Time Histories at Various Points on Rectangular Structure Subjected to Loading as Shown in Figure 2-6, Case 1 (Soft Backfill)	38
2-10	Displacement-Time Histories at Various Points on Rectangular Structure Subjected to Loading as Shown in Figure 2-6, Case 2 (Stiff Backfill)	39
2-11	Vertical Stress-Time Histories at Soil-Structure Interface Above and Adjacent to Transverse Centerline of Rectangular Structure, Case 1 (Soft Backfill)	40
2-12	Vertical Stress-Time Histories at Soil-Structure Interface Above and Adjacent to Transverse Centerline of Rectangular Structure, Case 2 (Stiff Backfill)	41
2-13	Vertical Stress-Time Histories at Soil-Structure Interface Above and Adjacent to Longitudinal Centerline of Rectangular Structure, Case 1 (Soft Backfill)	42
2-14	Vertical Stress-Time Histories at Soil-Structure Interface Above and Adjacent to Longitudinal Centerline of Rectangular Structure, Case 2 (Stiff Backfill)	43
3-1	Assumed Collapse Modes (Yield Lines) for Reinforced Concrete Slab	53
3-2	Resistance Function for a Reinforced Concrete Slab Support Cases 2, 3, 4, 6 and 7	54

LIST OF FIGURES (CONTINUED)

Figure No.		Page
3-3	Airblast Overpressure Measured in HEST Cavity. HEST Test on Structure 3B, August 1977	55
3-4	Interface Stress Exerted by Soil on Roof of Structure 3B. HEST Test on Structure 3B, August 1977	55
3-5	Displacement-Time History for SDOF Model (4 Different Damping Ratios) and for Midpoint of Roof for Structure 3B ($\ell/h = 10$) Subjected to Measured Interface Stress-Time History	56
3-6	Resistance-Deflection Path for SDOF Model of Structure 3B, Including 20 Percent Critical Damping, Subjected to Measured Interface Pressure Loading	57
3-7	Displacement-Time History for Structure 3B (Thin Box $\ell/h = 10$) Applied Load Based on HEST Overpressure	58
3-8	Displacement-Time History for Structure 3D (Thick Box $\ell/h = 4$) Applied Load Based on Interface Pressure for Structure 3B	59
3-9	Displacement-Time History for Structure 3D (Thick Box $\ell/4 = 4.4$) Applied Load Based on HEST Overpressure	60
4-1	Shell Embedded in an Elastic Continuum	68
4-2	Coupling of Shell and Cavity	69
4-3a	Response of n = 2 Mode, M = .34	70
4-3b	Response of n = 2 Mode, M = 1.0	71
4-4	Damping Ratio for Various Mass Ratios	72
4-5	Frequency Ratio for Various Mass Ratios	73
I-1	Geometry of Slab Used to Determine Optimum Discretization for Roof	79

LIST OF FIGURES (CONTINUED)

Figure No.		Page
I-2a	Mode 1 of Roof Slab; Three Elements Through Thickness ω = 146.64 Hz	80
I-2b	Mode 1 of Roof Slab; Two Elements Through Thickness ω = 146.65 Hz	80
I-3a	Mode 2 of Roof Slab; Three Elements Through Thickness ω = 267.30 Hz	81
I-3b	Mode 2 of Roof Slab; Two Elements Through Thickness ω = 267.32 Hz	81

LIST OF TABLES

Table No.		Page
2-1	Material Properties Used in Transient Analysis of Rectangular Structure	44
2-2	Calculated and Measured Frequencies of Rectangular Structure 3D ($\ell/h = 4$)	45
2-3	Fraction of Critical Viscous Damping from Calculations of Free Vibration of Buried Rectangular Structure ($\ell/h = 4$)	47
I-1	Frequencies of Roof Slab (Hz)	82

ABBREVIATIONS AND SYMBOLS

a	shell radius
c_s, c_p	shear, dilatational wave speeds
c	viscous damping coefficient
E, G	Young's and shear moduli, respectively
F	applied force
h	thickness of slab or shell
k	generalized stiffness
k_n	modal stiffness
ℓ	span
ℓ_L, ℓ_S	long and short spans of a rectangular slab, respectively
m	generalized mass
M, N	mode numbers for thin plate
n	mode number for cylindrical shell
P	internal resisting force
q	resistance of single-degree-of-freedom idealization of a slab
q_n	generalized coordinate of embedded cylindrical shell
r	radial coordinate
T, V	kinetic, potential energies of shell
u_n	modal radial displacement
x, $\dot{x}$, $\ddot{x}$	displacement, velocity, acceleration
y	deflection of a single-degree-of-freedom idealization of a slab
w, v	radial tangential displacements, respectively, of cylindrical shell
ζ	ratio of damped frequency of shell to in vacuo, undamped frequency
η	damping ratio
λ	$K - \frac{2}{3} G$
ν	Poisson's Ratio
ρ	mass density
ρ'	mass density of cylindrical shell
σ	stress
μ	mass per unit area
ω	natural frequency
Ω	nondimensional frequency = $\frac{a\omega}{c_s}$

SECTION 1

INTRODUCTION

1.1. BACKGROUND

Forced vibration tests were conducted on a model buried arch and on two buried rectangular structures at the site of the ESSEX Phase 3 Event near Fort Polk, Louisiana. The tests on the arch were the subject of a previous theoretical study (Reference 1) which investigated how resonance was suppressed when the structure was covered with backfill. A series of finite element analyses showed that radiation damping was significant for the prevailing backfill conditions, and that the amount of radiation damping varied from about 10 to 20 percent of critical over a reasonable range of backfill wave speeds. The present study considers the response of the rectangular structures from a similar viewpoint.

The geometry of the rectangular structures and backfill and instrumentation layout are shown in Figures 1-1 and 1-2. These structures were subjected to forced vibration testing after the ESSEX Phase 3 Event. The original backfill was excavated, the structures were inspected and found to be undamaged. Forced vibration tests were conducted first on the uncovered structures. Then sand backfill was placed by raining from a height of 5 feet and the tests were repeated. The tests and results are described in detail in Reference 2. Typical results of the tests are shown in Figures 1-3 and 1-4 in the form of impedance (F_{max}/v_{max}) and quadrature (F_{max} times peak acceleration times sine of the phase angle between them) versus frequency. When the driving frequency approaches a natural frequency of the structure, there is a valley in the impedance plot (large v_{max}) and a peak in the quadrative plot (large peak acceleration). One observation is that the stiffer structure, 3D ($\ell/h = 4$), exhibits resonance for both the covered and uncovered conditions. In contrast, the covered arch exhibited no resonance at all and the covered rectangular structure, 3B ($\ell/h = 10$), exhibited weak resonance. The second surprising result is that the resonant frequencies of the covered structure are almost identical to those of the same structure without backfill. This conflicts sharply with the results of modal analysis of protective structures in soil which shows that, if the soil is assumed to

be bonded to the structure, the addition of soil mass to the structure decreases its embedded frequencies relative to those in vacuum. Analytic results obtained from the arch show this, but they cannot be confirmed because resonant frequencies were not observed for the physical structure.

Analysis of free vibration of the covered arch showed that the amount of radiation damping varied from about 10 to 20 percent of critical, depending on the wave speed assumed for the backfill. Since the seismic wave speed for the sand is reported as being 30 to 45 percent of that for the compacted native backfill, it is anticipated that the radiation damping for the rectangular structures is less than that for the arch. This would help to explain why resonance was suppressed in the arch and not in the rectangular structures, and hence is one of the main subjects of the present study.

The observations that resonance appears in the covered case of rectangular structure 3D, that it is muted in the case of rectangular structure 3B and that it is completely suppressed in the case of the covered arch signify that frequency and damping parameters for equivalent single-degree-of-freedom (SDOF) models cannot easily be obtained from forced vibration tests without further analysis. The results also point out that deformational modes are strongly influenced by local backfill conditions and that knowledge of the effects of backfill is essential to accurate analytic modeling.

1.2. OBJECTIVE

One objective of the present study is to investigate the effect of variations in backfill wave speed on radiation damping for the rectangular structure, 3D ($\ell/h = 4$), and to evaluate equivalent fractions of critical viscous damping. Structure 3B is much stiffer than the arch and represents radiation damping in the high frequency range of deformational modes. The second objective is to use the damping values in an equivalent SDOF model subjected to airblast from a hypothetical explosion in order to determine the effect of including radiation damping on the response.

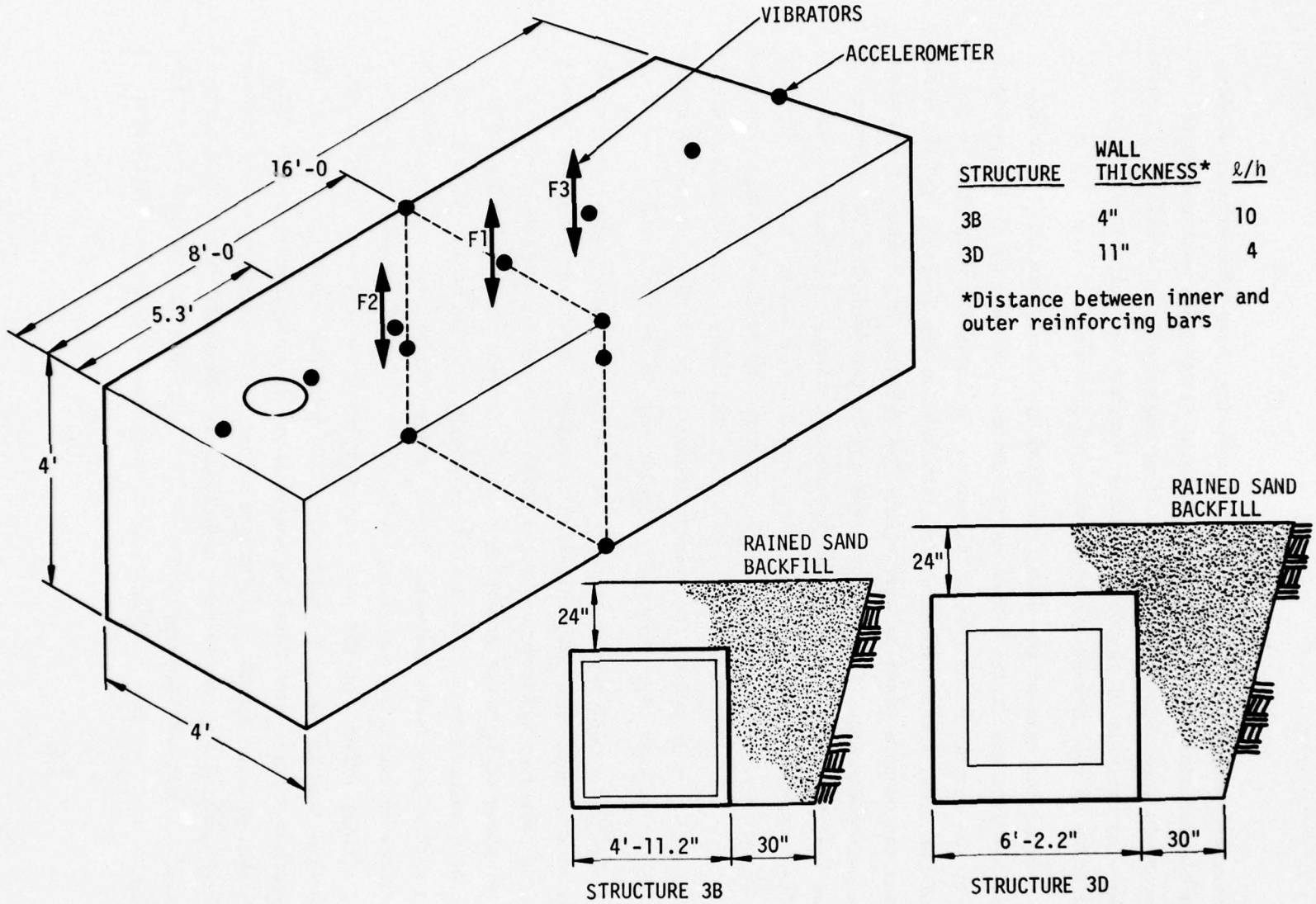
1.3. SCOPE

A study was made of the effect of backfill on the response of a rectangu-

lar structure subjected to transient loading using three-dimensional, elastic finite element simulation techniques. Natural frequencies and mode shapes of the structure were obtained before and after emplacement of backfill. Dynamic step-by-step analysis of transient loading designed to excite lower deformational modes of the covered structure was also performed.

As in the case of the arch, the chief hypothesis was that assuming stiffer backfill has little effect on the natural frequencies of deformational modes of the structure and that it increases the radiation damping. In the case of the arch, a crude model of friction between the backfill and the structure was included in order to investigate the relative importance of friction and radiation damping. It was found that the latter dominates the response, so that friction was not included in the present study. In the previous study, the effect of hysteretic material damping was also considered and was shown to be small compared with radiation damping for the low amplitude excitation considered here and produced in the forced vibration tests. Accordingly, material damping was neglected in the present study; in other cases where the stress level in the soil is higher material damping should be considered.

Nonlinear SDOF models of the roof slab for both rectangular structures 3B and 3D were developed using existing resistance functions reported in Reference 3. Membrane effects were considered, although the threshold displacement for these effects was not reached in the present analyses. The SDOF models were amended to include a viscous damping term whose coefficient was varied within the limits indicated by the finite element analyses to determine the effects of radiation damping on response of the roof. Since there were strong arching effects on the roof occurring during a HEST test on structure 3B, several loading functions were assumed in order to bound the possible range of responses. These were based on measurements of overpressure in the HEST cavity and on measurements of interface stresses. These studies were performed as nearly as possible as ordinary vulnerability analyses, except that a significant amount of viscous damping was assumed. In this way the effects of including or omitting radiation damping on targeting analysis are evaluated.



STRUCTURE	WALL THICKNESS*	ℓ/h
3B	4"	10
3D	11"	4

*Distance between inner and outer reinforcing bars

Figure 1-1. Rectangular Structure and Backfill Geometry.

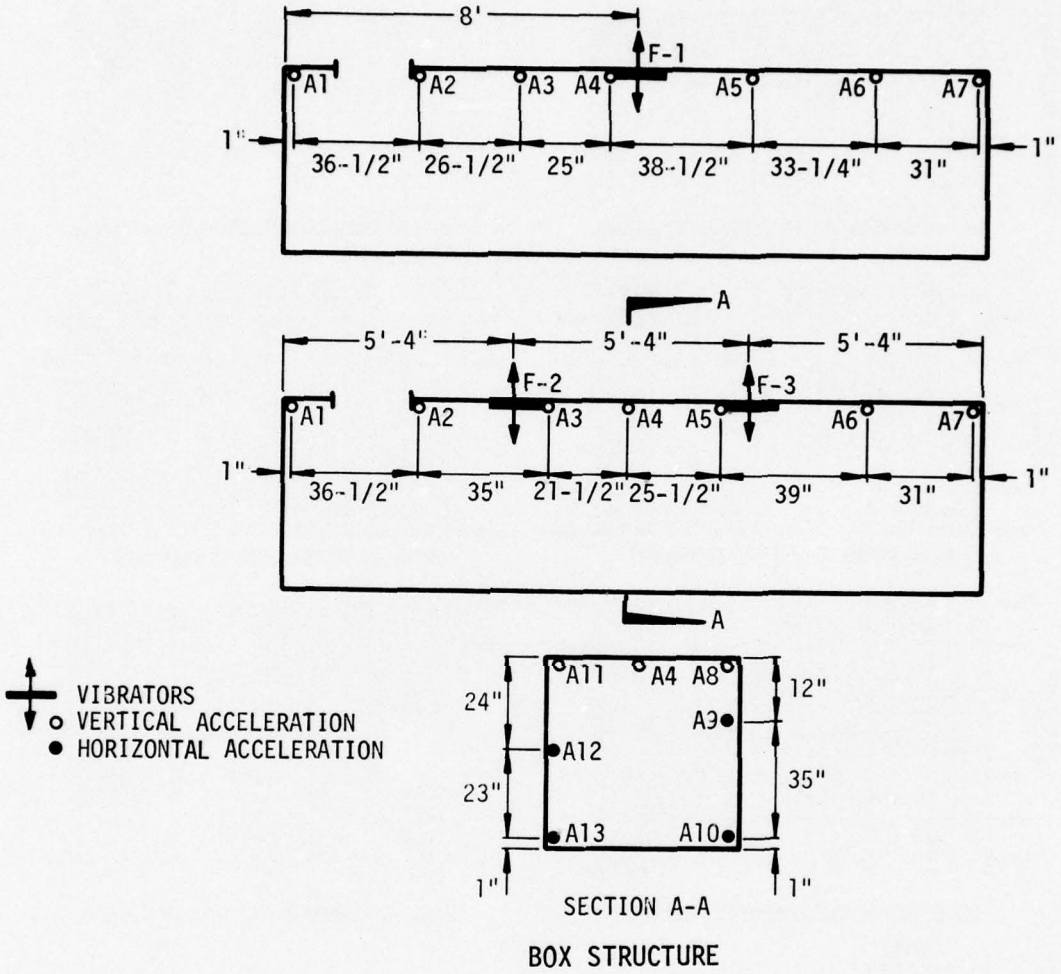
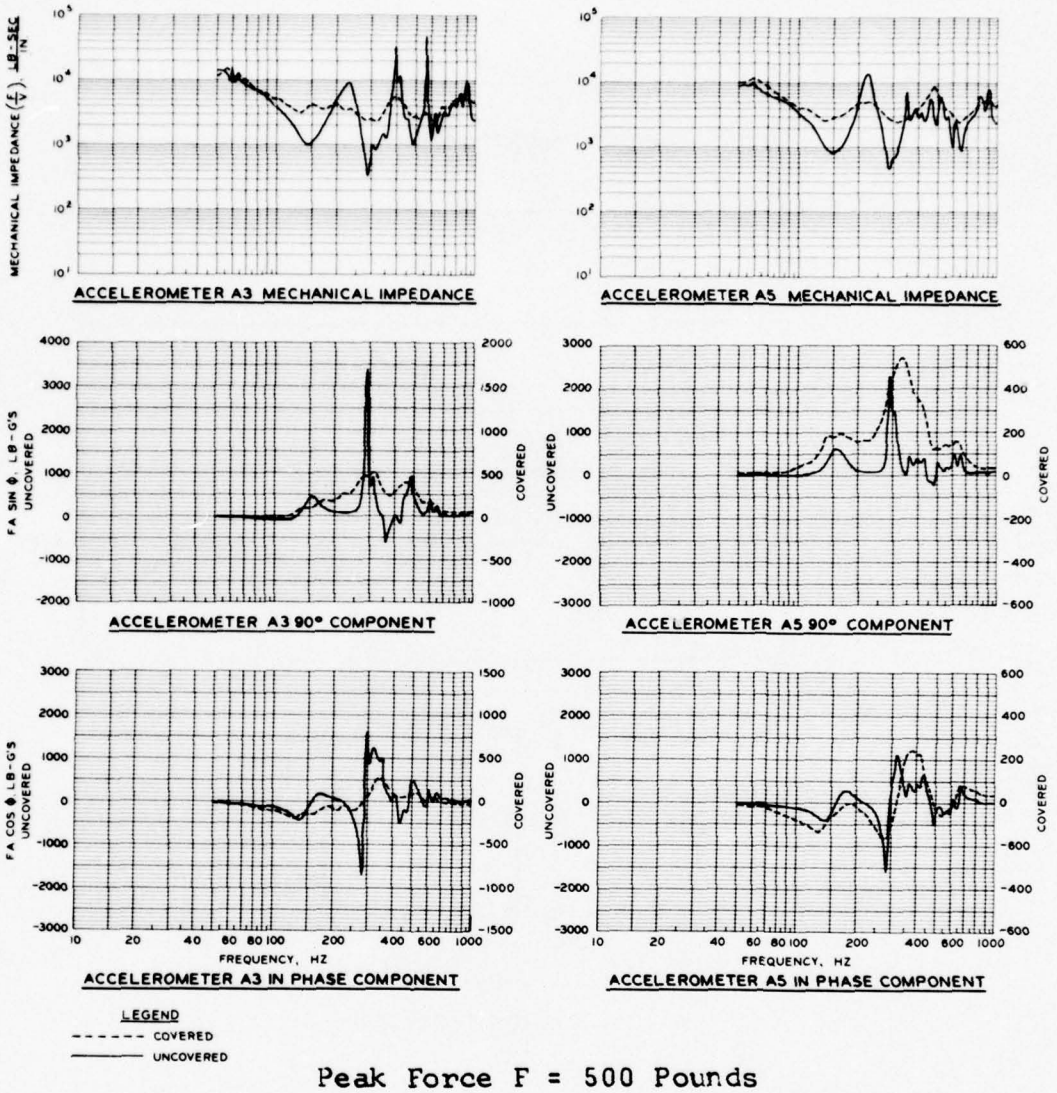
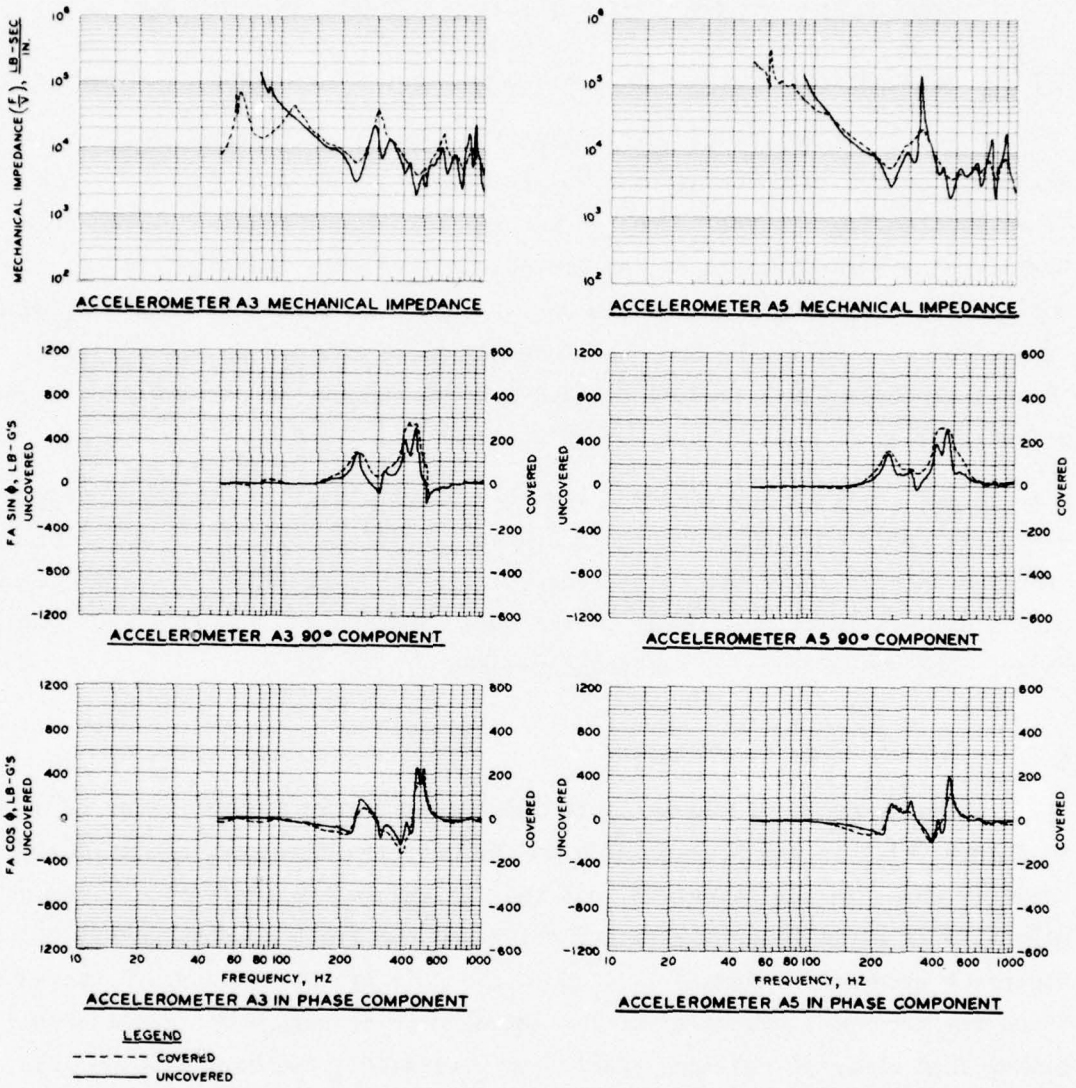


Figure 1-2. Geometry and Instrumentation for Arch and Rectangular Structures.



Peak Force F = 500 Pounds

Figure 1-3. Impedance and Quadrature for Rectangular Structures 3B Before and After Placement of Backfill Determined from Tests with Vibrators In Phase.



Peak Force F = 500 Pounds

Figure 1-4. Impedance and Quadrature for Rectangular Structure 3D Before and After Placement of Backfill Determined From Tests with Vibrators In Phase.

SECTION 2

FINITE ELEMENT SIMULATION OF BURIED RECTANGULAR STRUCTURE

2.1. INTRODUCTION

The first step in investigating the dynamic properties of the soil-structure system is to obtain natural frequencies and mode shapes for the lower deformational modes of the structure. Since the true soil-structure system is semi-infinite in extent, it does not possess classical normal modes. Nevertheless, a reasonable approximation to local deformational modes can be obtained by fixing the outer boundaries of the finite element grid. The calculated natural frequencies and mode shapes are compared with measurements in order to qualify the analytic model.

Next a transient response analysis using direct integration methods was performed. An energy-absorbing boundary condition of the Lysmer-Kuhlemeyer type was used at the subsurface boundaries of the soil island in order to simulate a semi-infinite soil domain. The wave speed in the backfill was varied to investigate the effects on radiation damping.

2.2. NORMAL MODES OF STRUCTURE

The geometry of the analytic model used in the present study is shown in Figure 2-1. If the access hatch in the roof is neglected, two planes of symmetry exist in the structure, and this is assumed in the finite element model. This elminates anti-symmetrical modes and frees computer capacity to represent accurately signals induced in the soil by vibration of the structure. Since the natural frequencies of the rectangular structure are considerably higher than those of the arch previously considered, the wave lengths are shorter and the required discretization is finer. The finite element discretization of the structure is shown in Figure 2-2. Hexahedral continuum elements are used for the structure as well as for the soil. As shown in Appendix I, a preliminary modal analysis of the roof was performed to determine optimum discretization; the same discretization was then adopted for the floor and walls.

The properties of the soil outside the backfill which are assumed in the analysis are based on initial tangent moduli, Reference 1. This is appropri-

ate for simulating cases of forced structure vibration because the strain amplitudes of signals reaching the soil are small. In the transient analyses, the properties of the backfill were varied over a range deemed appropriate to reasonable backfill conditions. In the modal analysis of the covered structure, the backfill properties are assumed on the basis of initial tangent moduli measured in laboratory tests on Cook's Bayou sand. The stress-strain data for the compacted native soil backfill and for Cook's Bayou sand are shown in Figure 2-3. The properties are summarized in Table 2-1.

The natural frequencies and mode shapes were obtained with a Rayleigh-Ritz procedure in which the initial shape functions were a set of orthogonal harmonic functions suggested by the theory of plates. Modes of the uncovered structure were computed by placing the structure in the excavation without any backfill. Modes of the covered structure were extracted by adding soil elements having the backfill properties assumed in Case 1. Table 2-2 compares natural frequencies of the analytic model with those measured in the forced vibration tests. There is good agreement only for the 237 Hz (214 Hz calculated) mode of the uncovered structure. There is fair agreement for the same mode of the covered structure (180 Hz calculated). It is significant that the calculated frequency of this mode is lower for the covered than for the uncovered case. This is due to the accession of soil mass to the structure which more than compensates for the added stiffness. However, the measurements show no change in frequency when backfill is added. The simplest explanation is that in the physical experiment the sand backfill does not follow the deflections of the structure due to arching and hence there is little or no accession of soil mass. In general, the measured frequencies are higher than those calculated. Several anti-symmetrical modes were also measured, which cannot be calculated with the present model. The mode shapes are illustrated in Figures 2-4 and 2-5.

2.3. TRANSIENT ANALYSIS OF COVERED STRUCTURE

The mechanism of damping which is considered in the present analysis is radiation associated with wave propagation in a semi-infinite domain. A Lysmer-Kuhlemeyer energy-absorbing boundary condition is imposed on subsurface boundaries of the soil island in order to approximate such a domain. About four velocity-time cycles in the first mode of vibration are complete before waves reach

the boundaries, at which point most of the signal is absorbed. Damping is investigated by observing decay in the amplitude of free vibration of various points on the structure. Motion is induced by applying a series of line loads to the roof, floor and wall of the structure as shown in Figure 2-6. This distribution corresponds roughly to the third deformational mode of the covered structure shown in Figure 2-5c, whose calculated frequency is about 180 Hz. The time history of the applied loads is a triangular pulse whose duration is equal to 0.0028 second (about the half period of the 180 Hz mode). The total duration of the calculations is 0.055 second, or about 20 times the duration of the applied load. This load distribution and time history produce a transient response which is strongly dominated by the 180 Hz mode, with the result that it is easier and more meaningful to interpret percent critical damping from the log decrement of displacements in successive cycles than if several modes affect the response. The load pattern is quite similar to the Ritz load function used to generate the 180 Hz mode in the extraction of normal modes.

The backfill properties considered in the present parametric study are summarized in Table 2-3. Case 1 corresponds to the best estimate of the properties in the physical experiment. Case 2 corresponds to backfill wave speeds twice those in Case 1.

2.3.1. Radiation Damping

The results of the transient vibration analyses are shown in Figures 2-7 and 2-8 in terms of velocity-time histories at the midpoints of the roof, floor and sidewalls. They show that as stiffer backfill is assumed, the peak velocity decreases slightly. A frequency shift is difficult to detect, because damping so dramatically reduces the late-time velocity in Case 2.

The fraction of critical damping is evaluated from the log decrement of peak displacement in successive cycles according to the expression:

$$\ell_n \frac{X_{n+1}}{X_n} = \delta = \frac{2\pi\eta}{\sqrt{1-\eta^2}}$$

where

X_n, X_{n+1} = peak displacements at cycle n, n + 1, respectively

η = fraction of critical damping

The displacement-time histories are shown in Figures 2-9 and 2-10. Since the transient response of the model is not purely harmonic, it is to be expected that the value of η will depend to a degree on where on the structure the peak displacements are observed and for which cycle. In order to obtain a representative value for the fraction of critical damping, it is estimated from two different cycles and at three locations.

The estimated fractions of critical damping are given in Table 2-3. They show that, for the backfill properties based on the initial tangent moduli for Cook's Bayou sand, damping is about 15 percent of critical. This is slightly greater than the damping (12 percent) obtained for the buried arch based on tangent moduli for native compacted backfill. Table 2-3 also shows that, for backfill properties based on two times the recommended initial Cook's Bayou moduli, the damping increases to about 22 percent of critical. This is also more than the comparable value for the buried arch (17 percent).

The finding that the equivalent fraction of critical damping is calculated to be higher for the rectangular structure than for the arch is surprising in view of the fact that the assumed backfill is stiffer for the arch. The finding also tends to conflict with the experimental observation that resonance was observed during forced vibration of the rectangular structure (suggesting low damping) whereas resonance was suppressed in the arch (suggesting higher damping). Other factors may have played an important role, as is discussed below.

The values of critical damping obtained in this analysis are consistent with those obtained for a more flexible, buried rectangular structure, Reference 4. There, the dynamic load factor for the response of the structure to a simulated airblast was calculated. A single-degree-of-freedom model having the same frequency characteristics was developed and viscous damping was increased until the same dynamic load factor was obtained, which occurred at fractions of critical damping between 20 percent and 40 percent. The values obtained in the present study are at the low end of this range, which is consistent with the lower wave speeds assumed here (550 fps and 777 fps versus 1,500 fps in Reference 4).

A question arises whether radiation damping which is measured over several cycles is relevant to targeting analysis of protective structures in which monotonically increasing deflections are of principal interest. Radiation damping of deformational modes occurs when deformations of the structure induce stress and velocity gradients in the adjacent soil which are propagated away in the form of waves. A crucial element in radiation damping is for the structural members to do work on the soil so that energy of vibration leaks out of the structure. For the case of airblast loading on the roof of the structure, it is clear that the principal responses of the walls and floor during the first quarter cycle arise from deflections and rotations which are compatible with the roof deformation. This statement needs to be qualified in the case of a high speed backfill where the downward traveling wave exerts appreciable stress on the sidewall during the period of interest. We restrict the discussion of the first quarter cycle of the lowest roof bending mode, Figure 2-5c, and to low wave speed backfill. The soil does work on the roof and the walls do work on the soil. If the soil beneath the floor is capable of following its inward motion, then the floor too does work on the soil. A SDOF model of the roof of the type used for targeting analysis considers only the roof slab, so that all of the work done by the soil on the roof remains as kinetic and internal energy of the roof. Leakage of energy through the walls and floor is neglected. Seen from this perspective, the first quarter cycle of loading is as much influenced by radiation damping effects as any other cycle. Furthermore, a simulation of the type shown in Figure 2-6 induces much the same pattern of deformations in the soil and structure as are induced by airblast loading on the roof. The fact that it requires several cycles to obtain a measure of the energy leakage is merely a nuisance, but the processes of energy leakage through the walls and floor are the same in later cycles as in the first quarter cycle. In the finite element simulation, the extent that leakage through the floor is exaggerated by the ability of the interface in the model to support tension, the analysis exaggerates radiation damping. In the opinion of the authors the degree of exaggeration is small in the cases which have been considered so far.

2.3.2. Arching

Arching is the phenomenon whereby the stress exerted on a buried

flexural member, such as a roof slab, varies across the span. Arching modifies the effective load on the member, and hence it is important in assessing vulnerability. Arching can occur due to dynamic interaction in elastic soil-structure systems and due to inelastic behavior of soils, especially those with a large friction angle. Although the present study was not aimed at investigating arching, the geometry of the problem is conducive to it. Accordingly, the interface stresses normal to the roof along its transverse and longitudinal centerlines were examined to see whether arching occurs. Cases of soft and stiff backfill are considered. The results of this examination are shown in Figures 2-11 through 2-14.

The variation in stresses along the transverse centerline for the soft backfill case is shown in Figure 2-11. Here, the stresses are highest in the center of the span and slightly lower toward the sidewall. A similar trend is observed for the stiff backfill case, Figure 2-12, in which damping reduces the frequencies of oscillation. In these cases the transverse variation in stress is negligible.

The variations in stresses along the longitudinal centerline for the soft and stiff backfill case are shown in Figures 2-13 and 2-14. These figures show, as do Figures 2-11 and 2-12, that the stresses are larger at the center of the span. The reason for this apparently is that the interface stresses vary with the velocities and displacements of the roof; since these are larger at midspan than at the supports, the stresses are also larger at midspan.

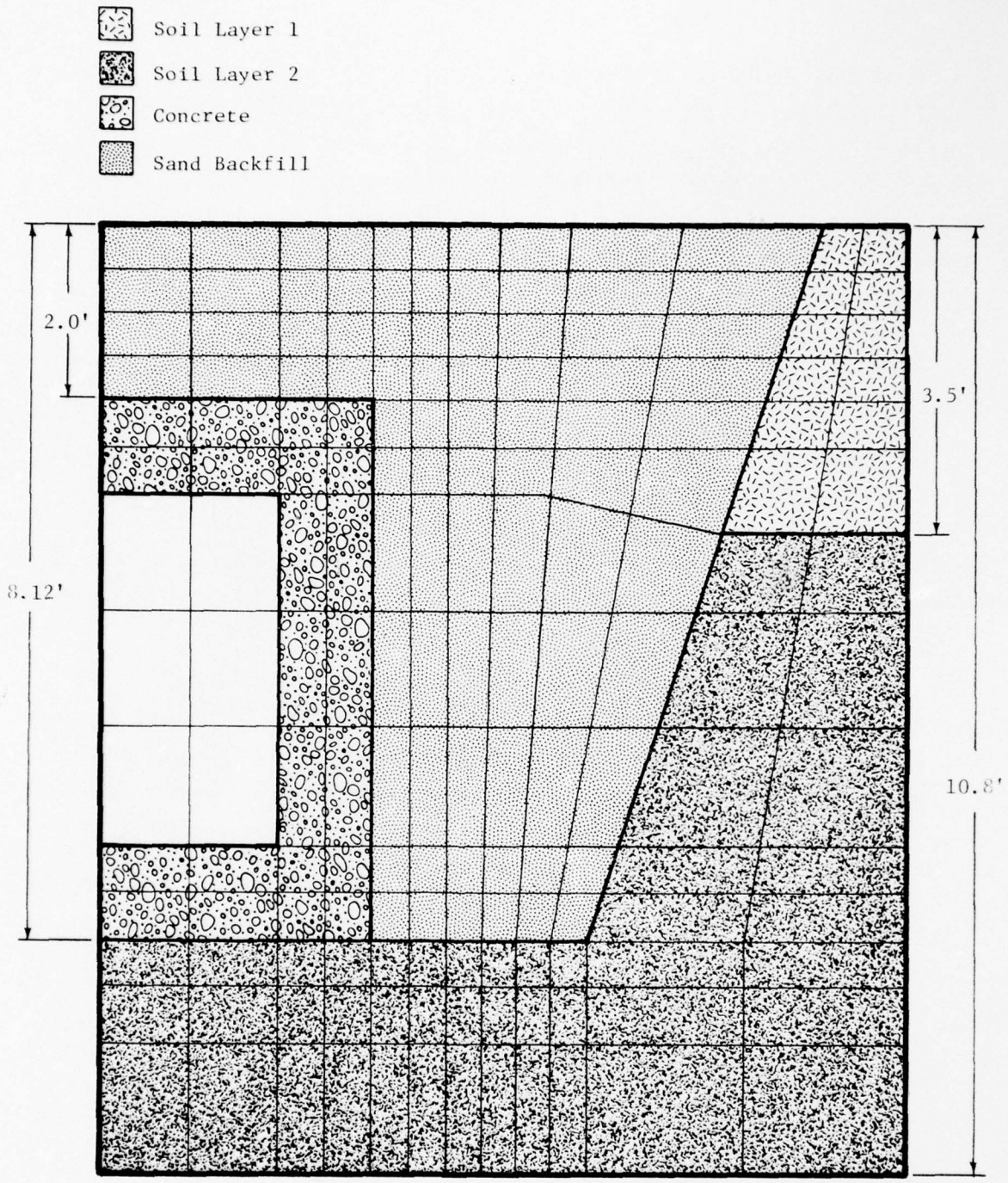


Figure 2-1. Elevation View of Transverse Section Through Finite Element Model of Rectangular Structure 3D.

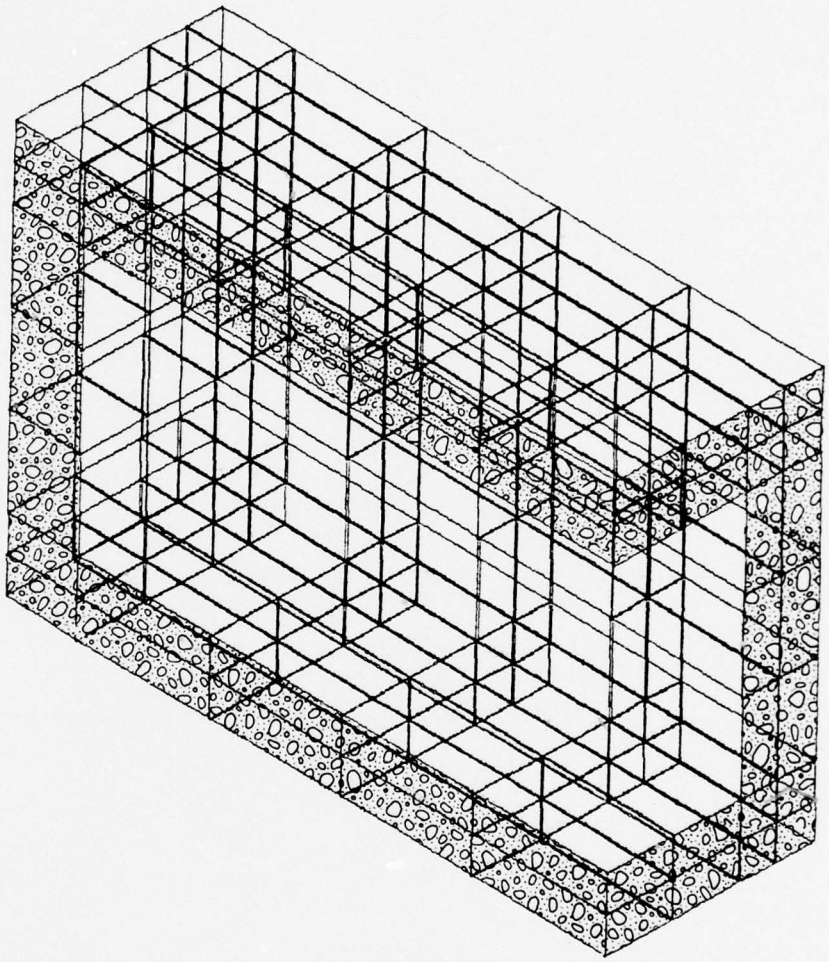


Figure 2-2. Finite element model of structure (for clarity, soil is not shown).

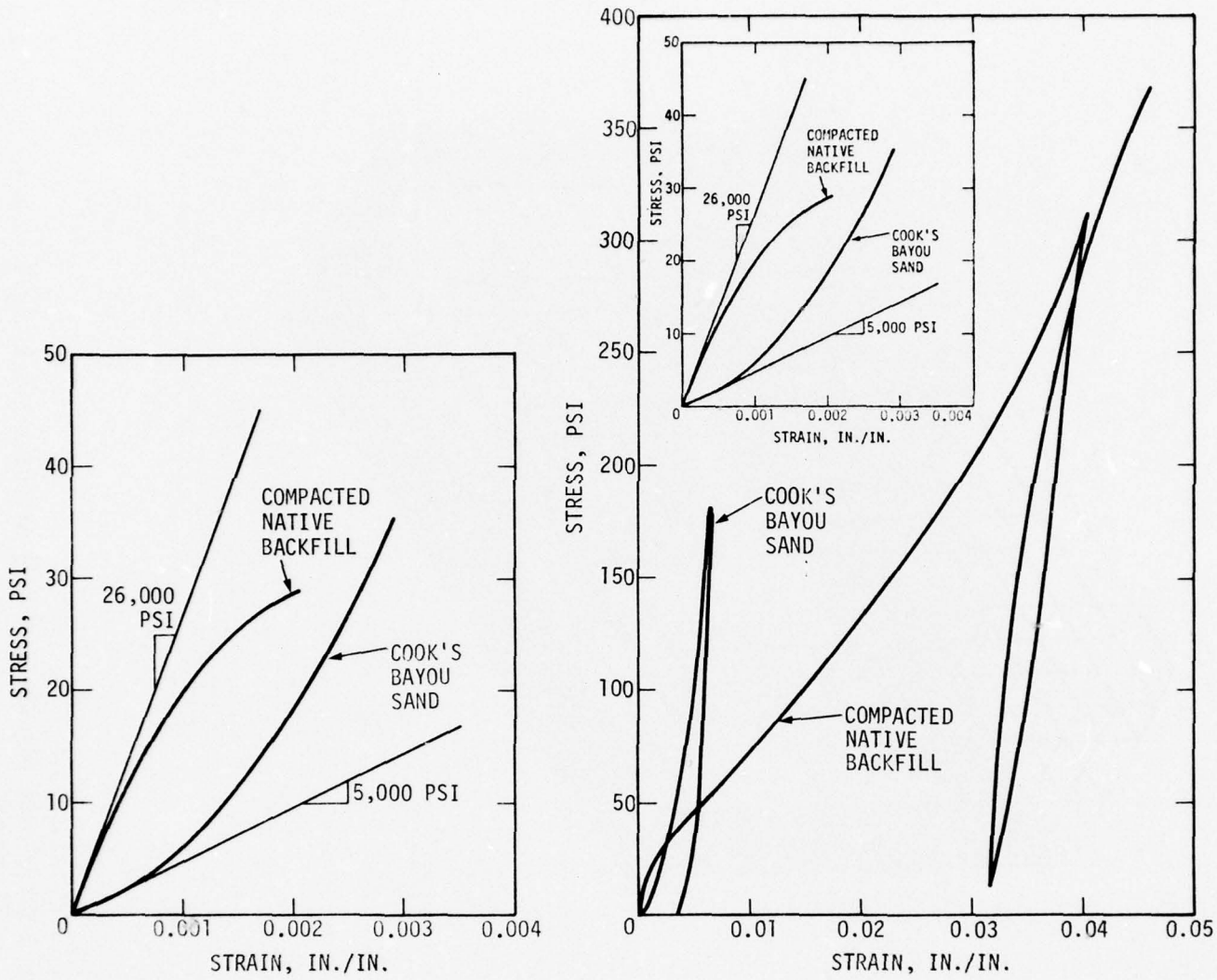


Figure 2-3. Uniaxial Stress-Strain Properties of Compacted Native Backfill (Arch) and Cook's Bayou Sand (Rectangular Structures).

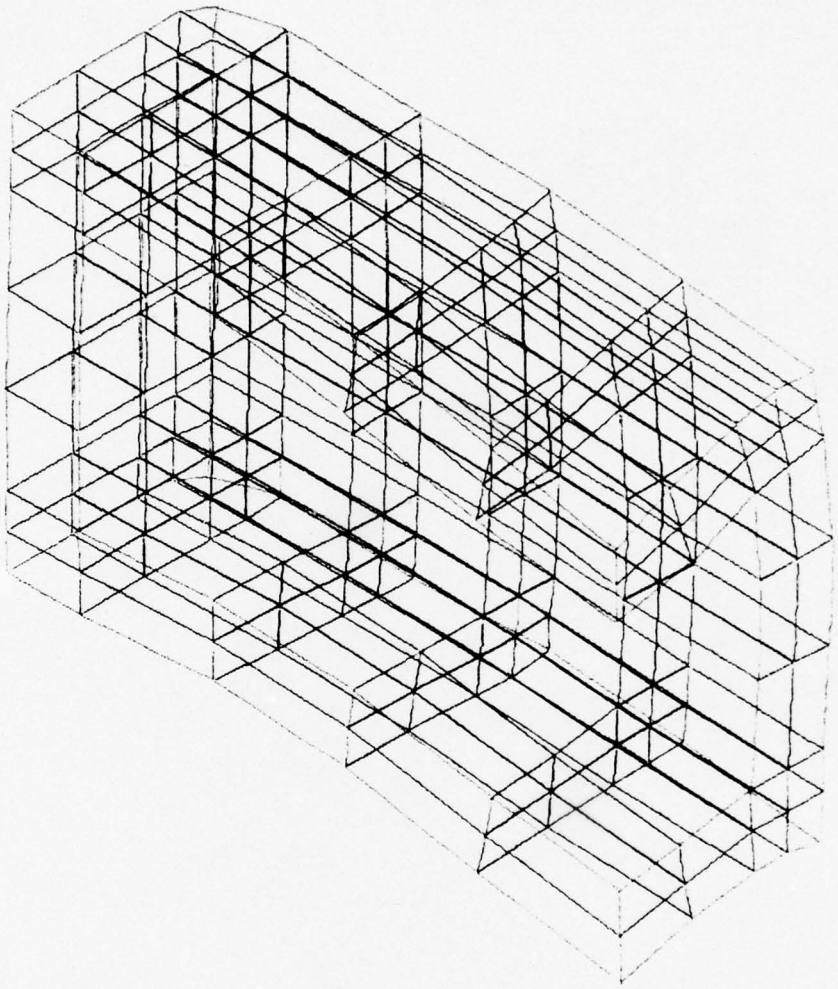
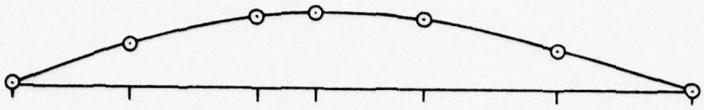
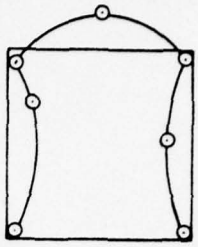


Figure 2-4a. Mode 1, 112 Hz (Uncovered).



237 Hz--Vibration in Phase



Measured Mode (Uncovered)

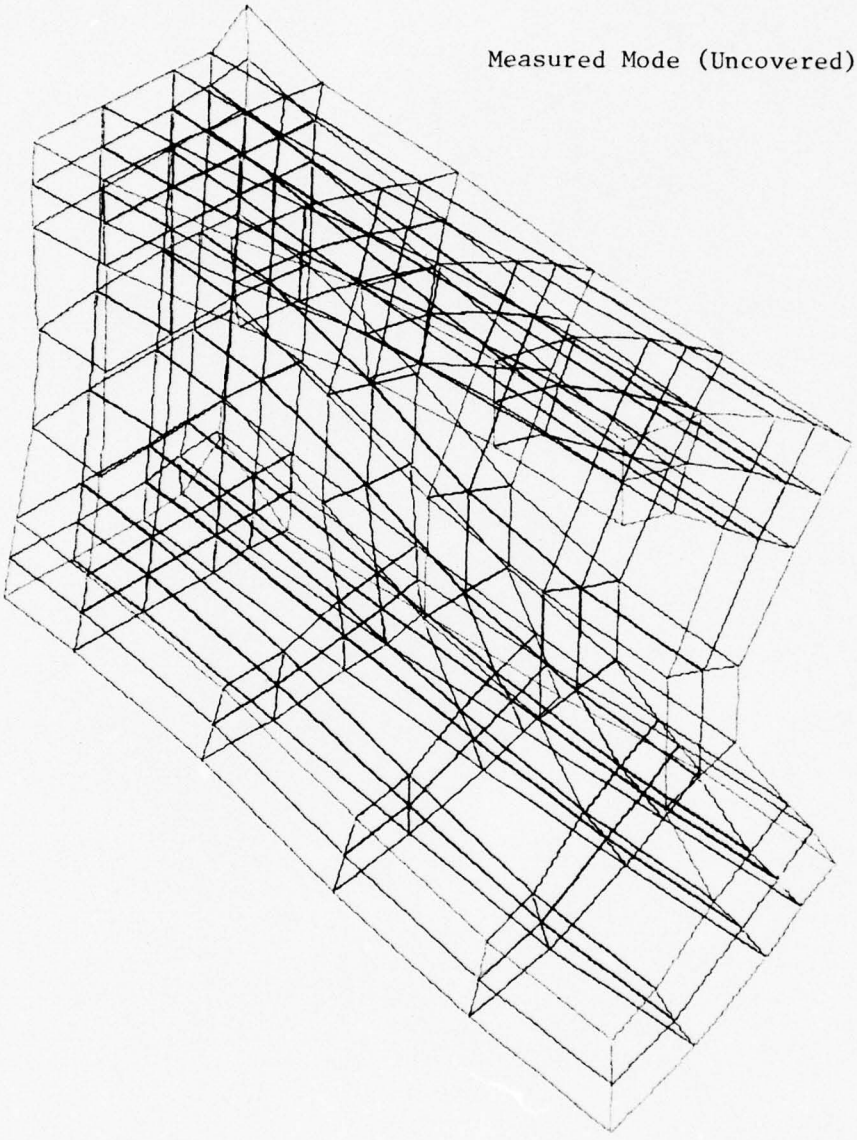


Figure 2-4b. Mode 2, 214 Hz (Uncovered).

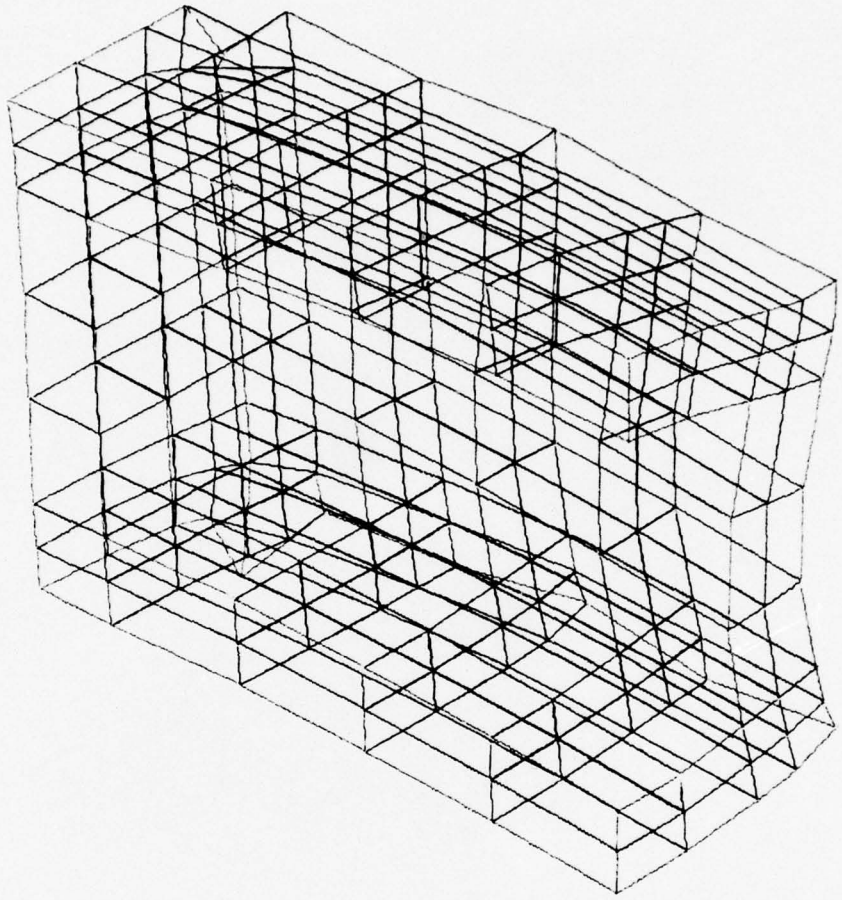


Figure 2-4c. Mode 3, 235 Hz (Uncovered).

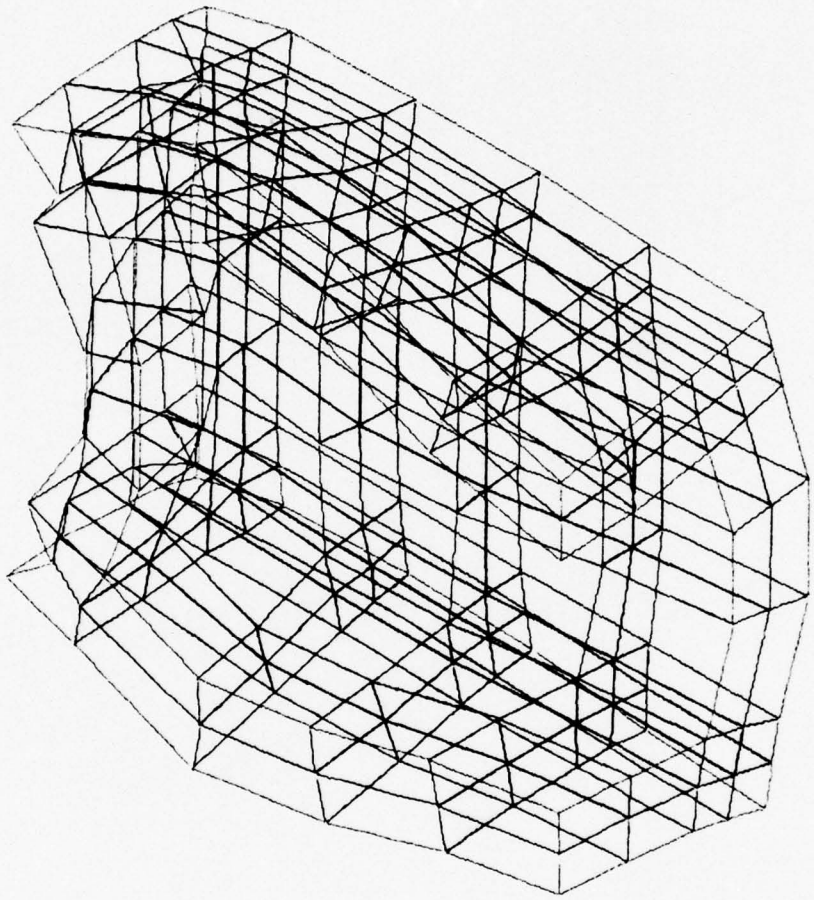


Figure 2-4d. Mode 4, 333 Hz (Uncovered).

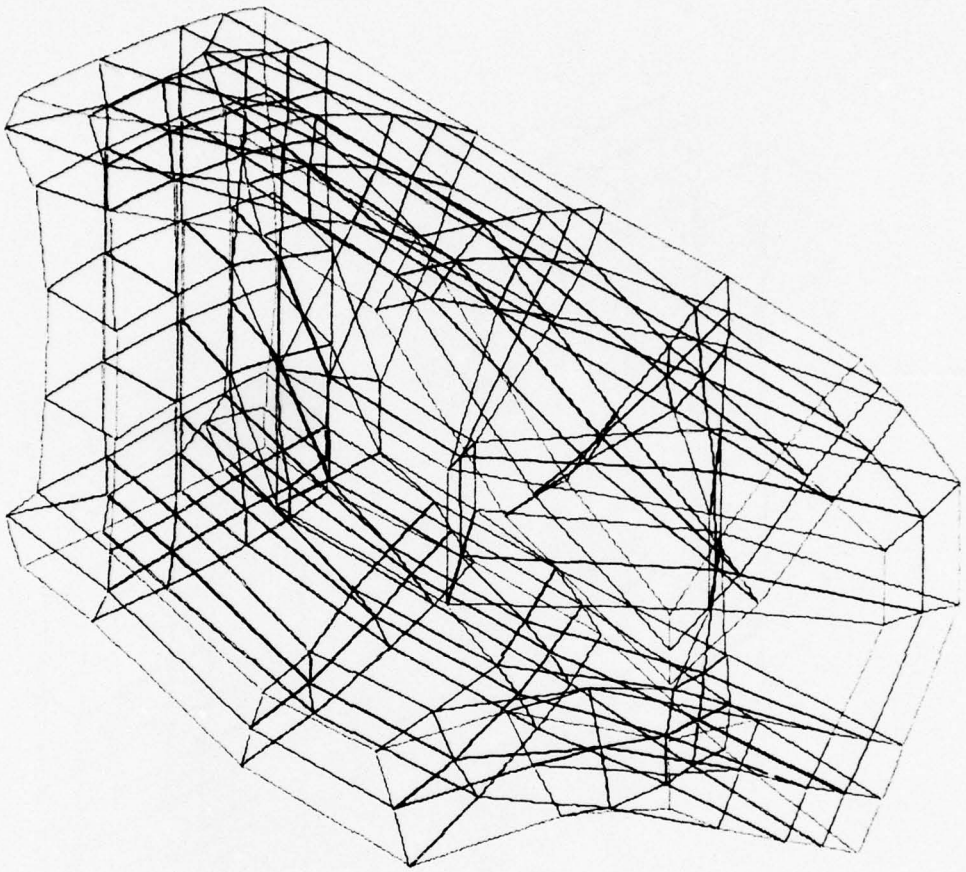


Figure 2-4e. Mode 5, 353 Hz (Uncovered).

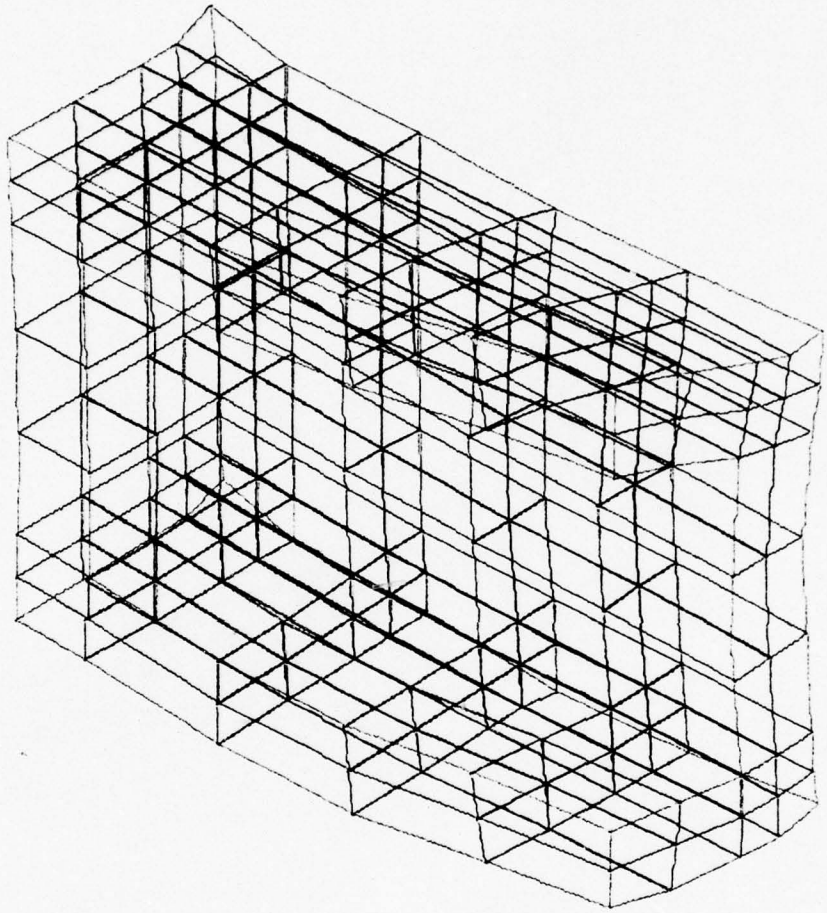


Figure 2-5a. Mode 1, 88 Hz (Covered).

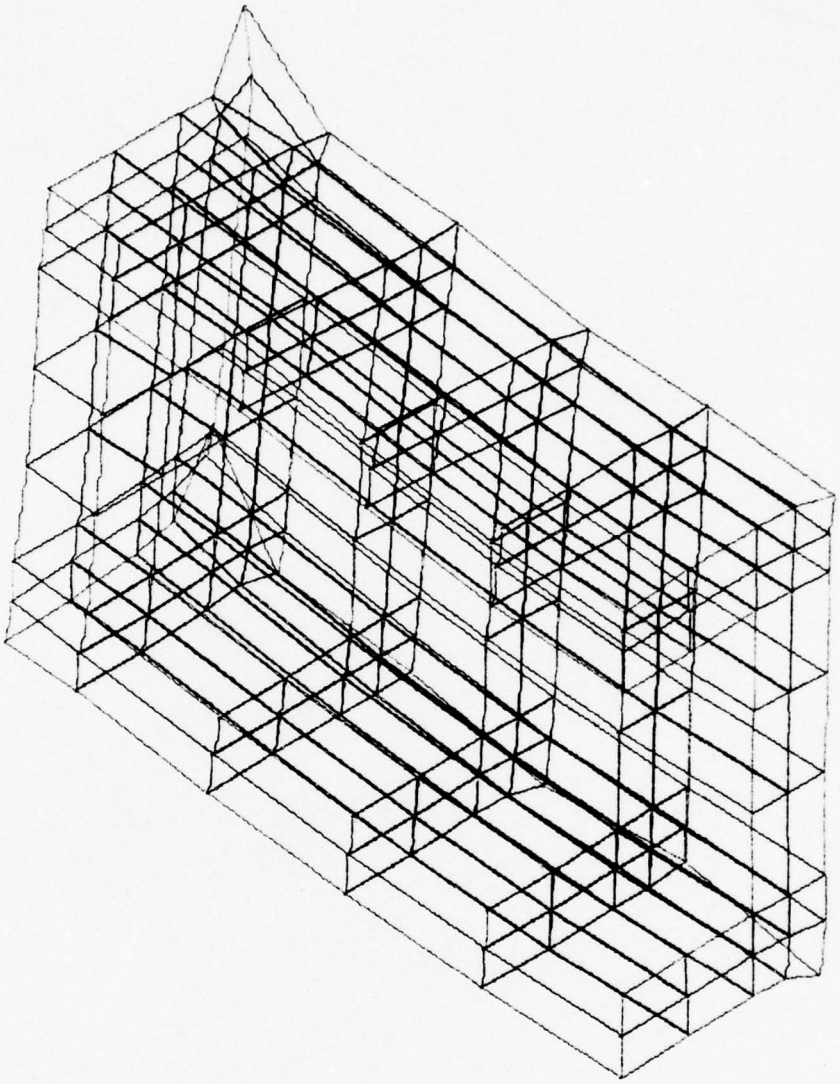
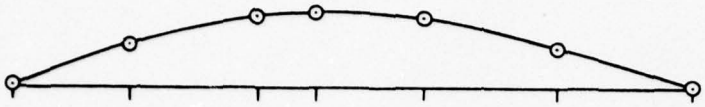
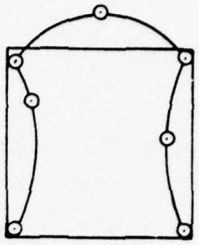


Figure 2-5b. Mode 2, 172 Hz (Covered).



237 Hz- Vibration in Phase



Measured Mode (Covered)

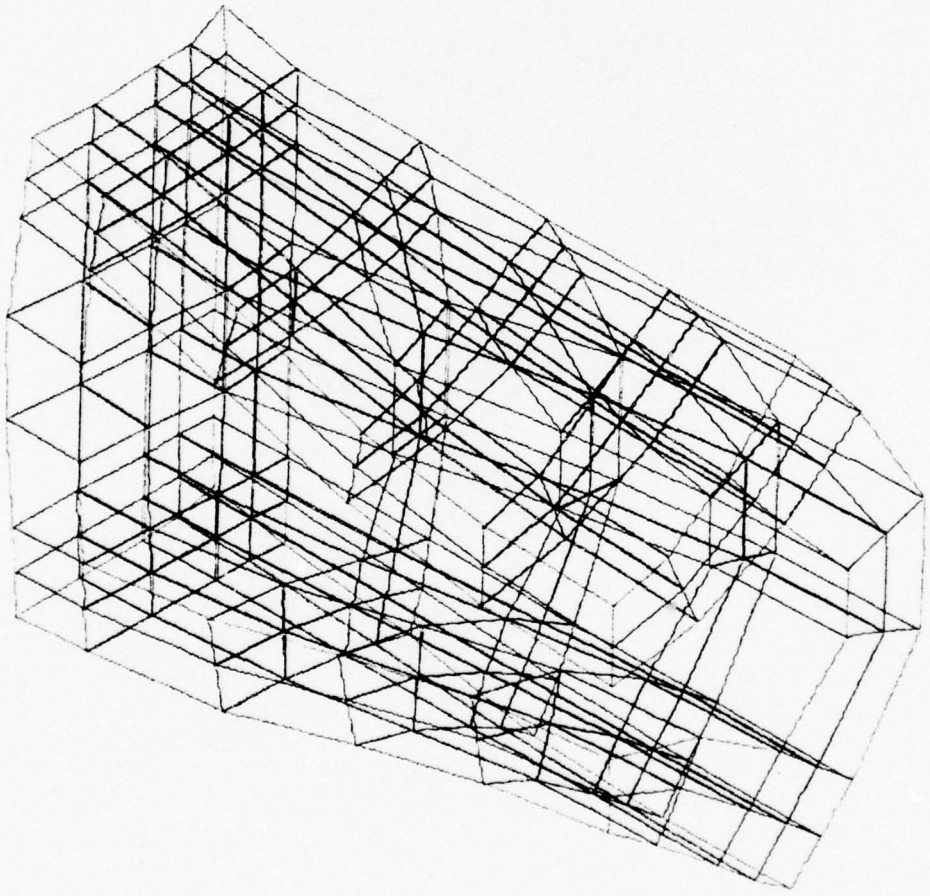


Figure 2-5c. Mode 3, 180 Hz (Covered).

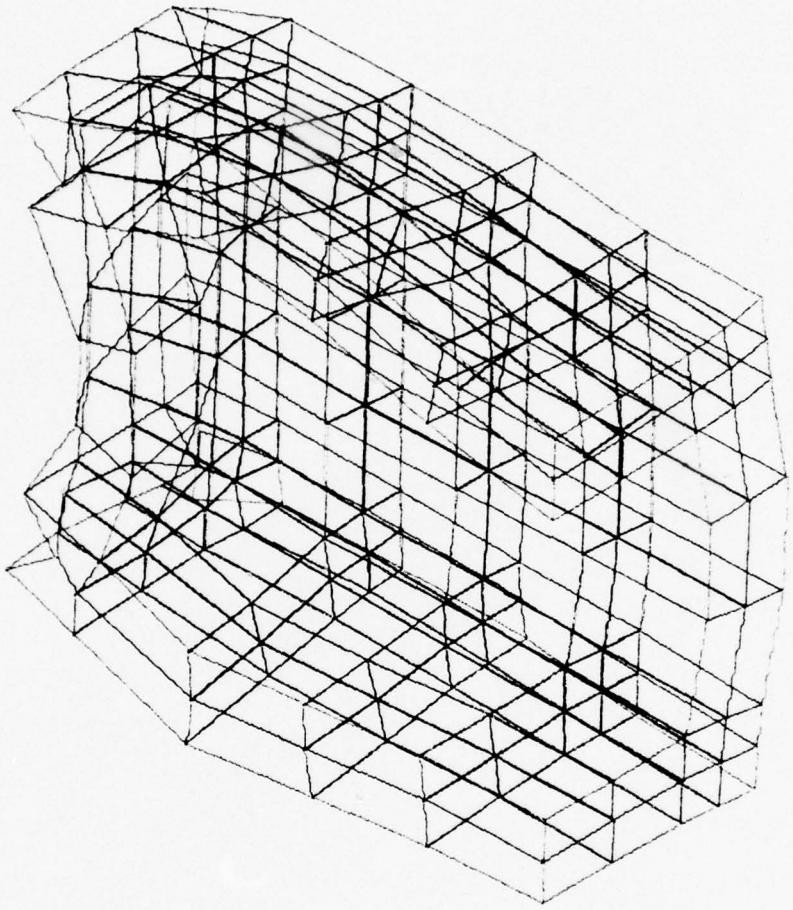


Figure 2-5d. Mode 4, 271 Hz (Covered).

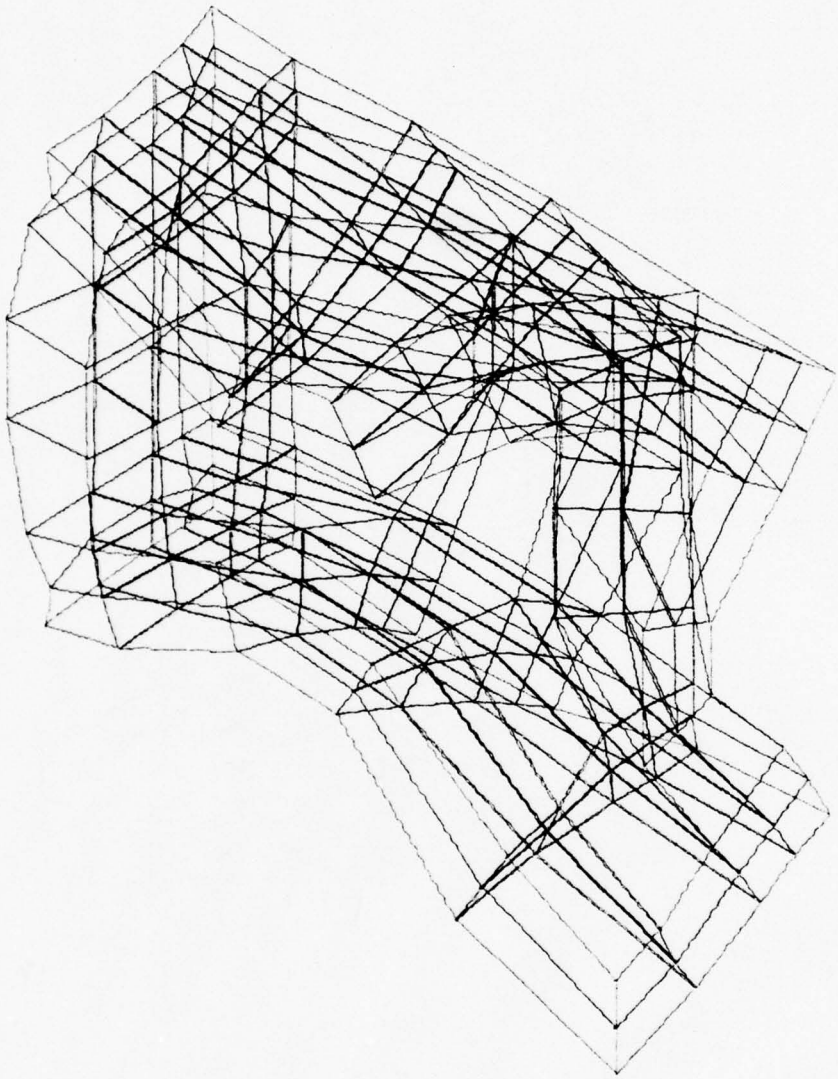


Figure 2-5e. Mode 5, 293 Hz (Covered).

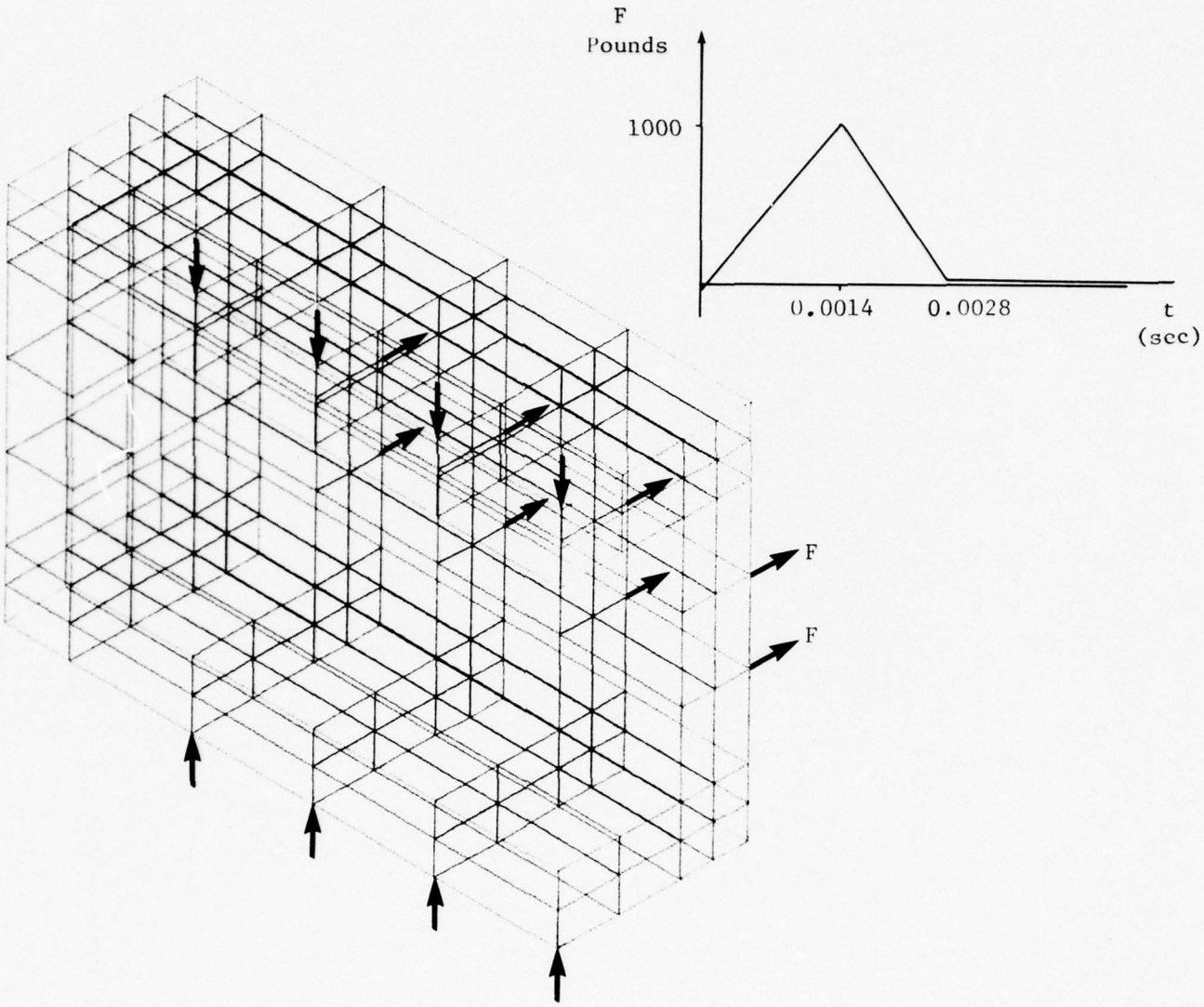


Figure 2-6. Loads Applied to Structure for Analyses of Transient Vibrations.

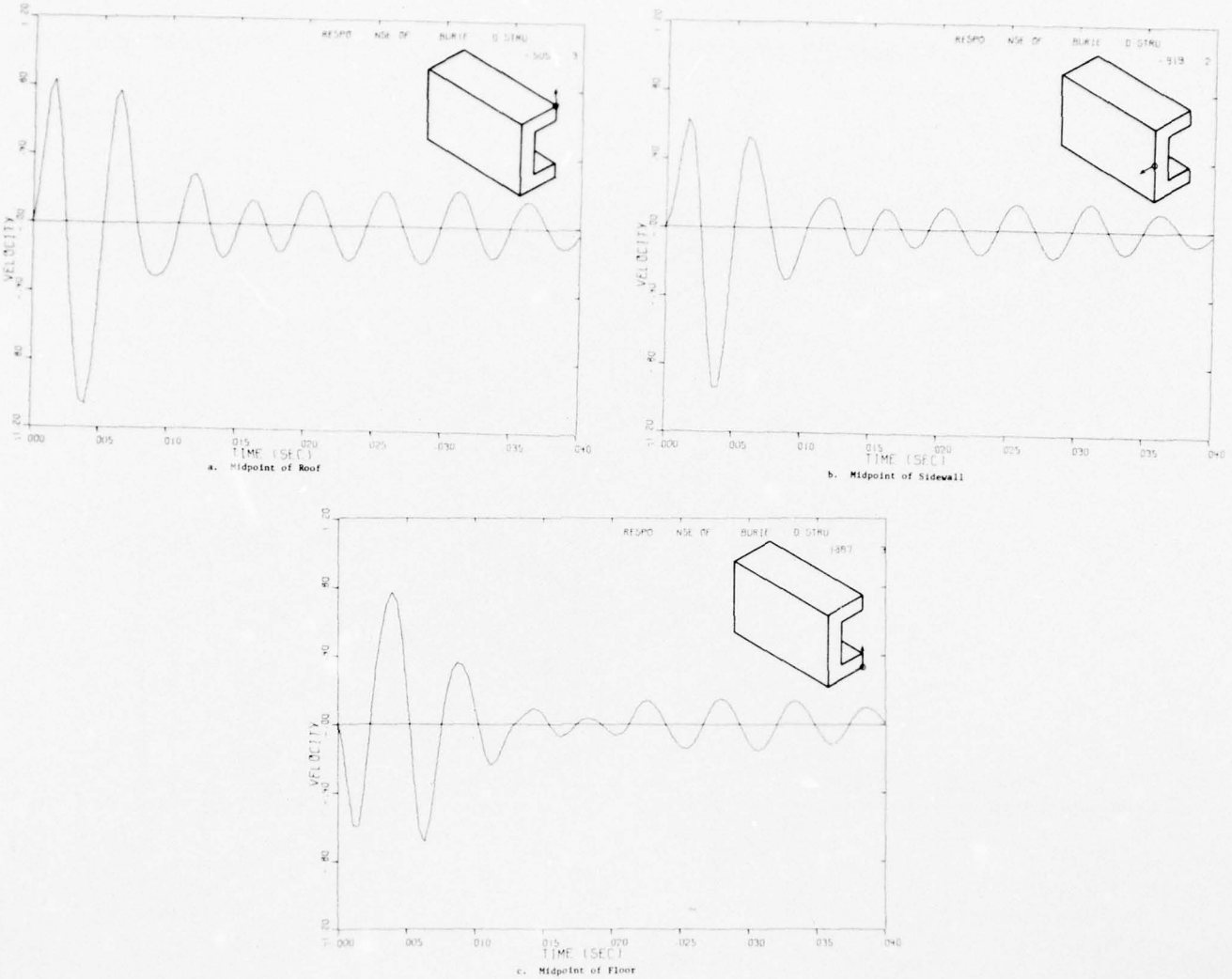


Figure 2-7. Velocity-Time Histories at Various Points on Rectangular Structure Subjected to Loading as Shown in Figure 2-6, Case 1 (Soft Backfill).

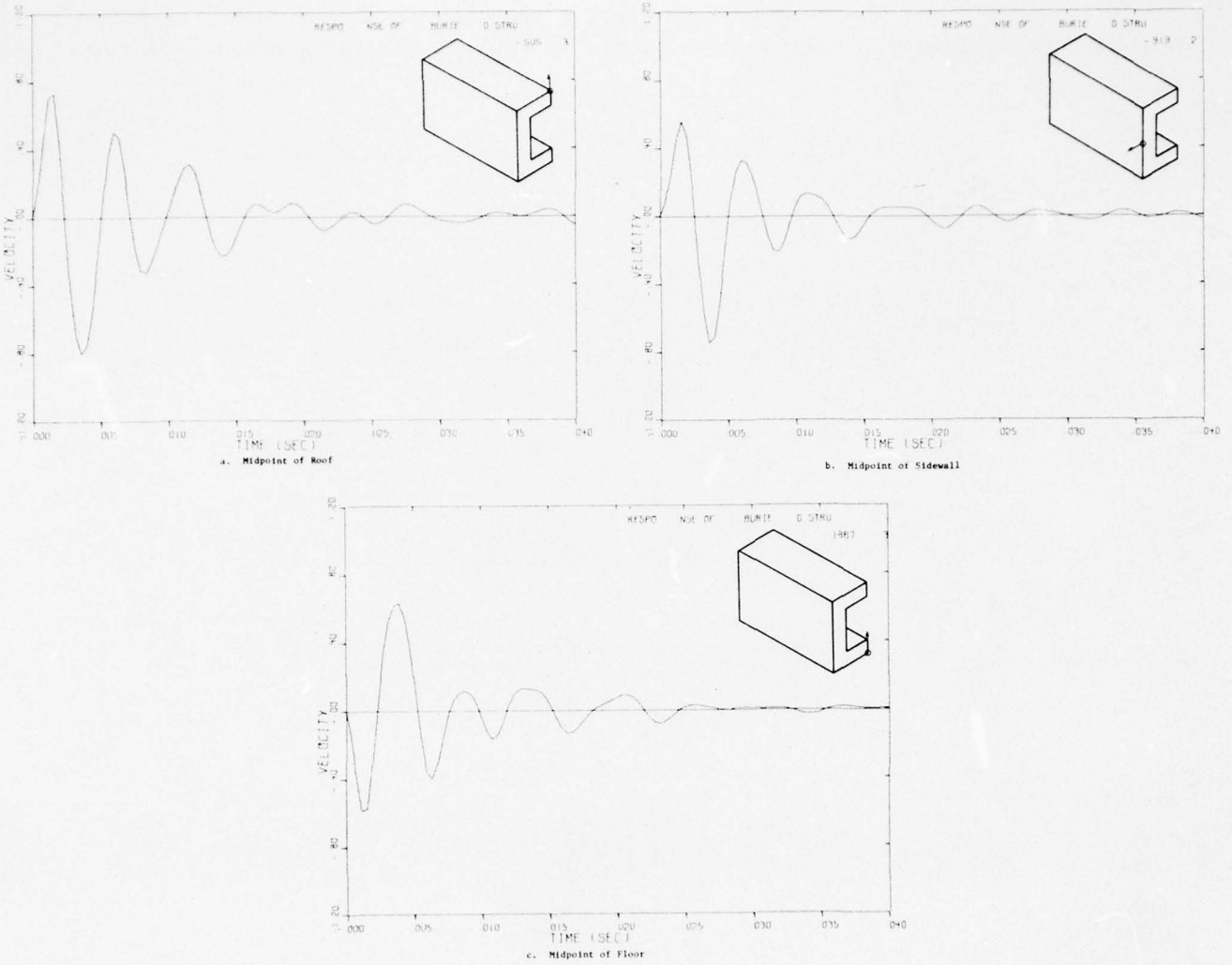


Figure 2-8. Velocity-Time Histories at Various Points on Rectangular Structures Subjected to Loading as Shown in Figure 2-6, Case 2 (Stiff Backfill).

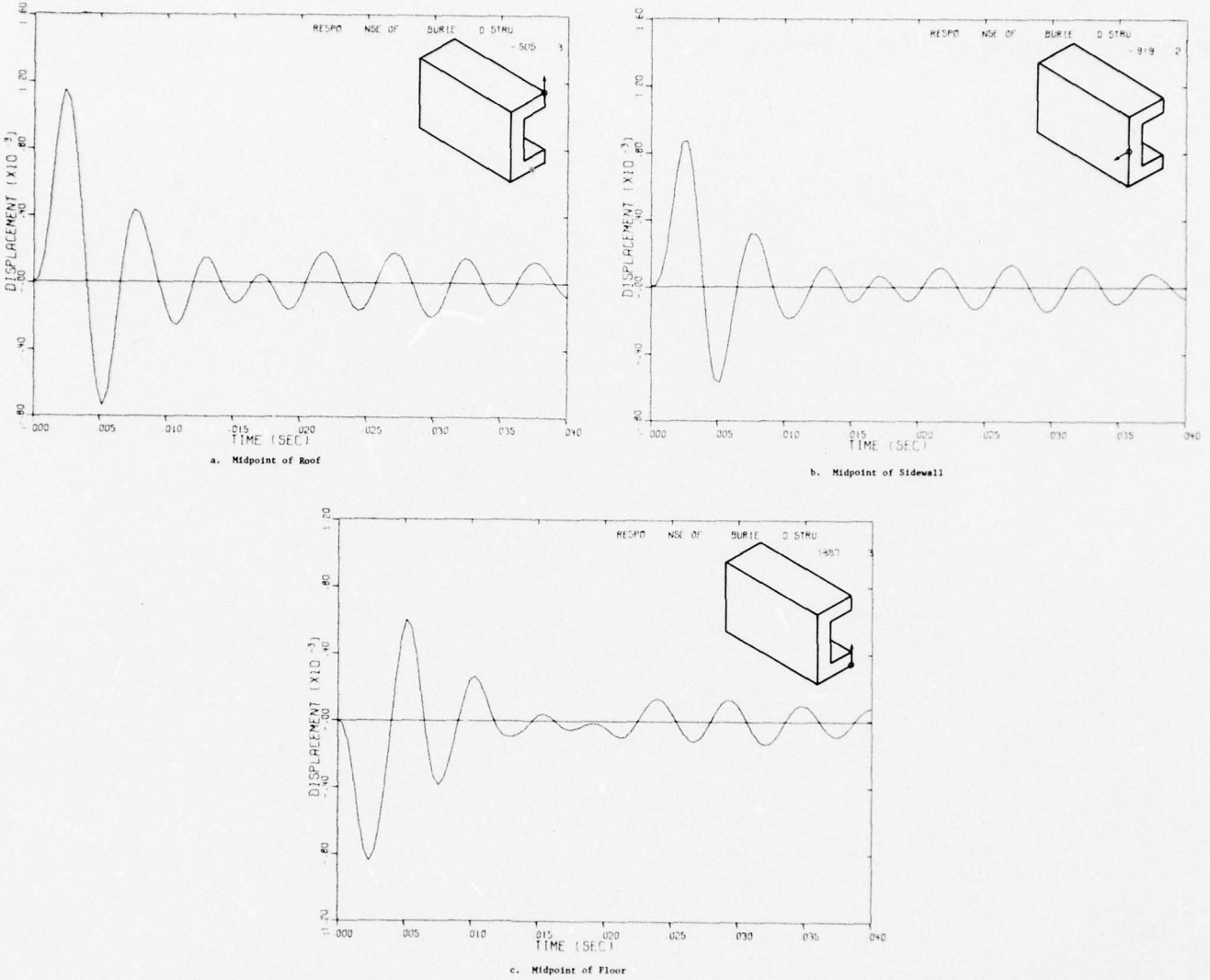
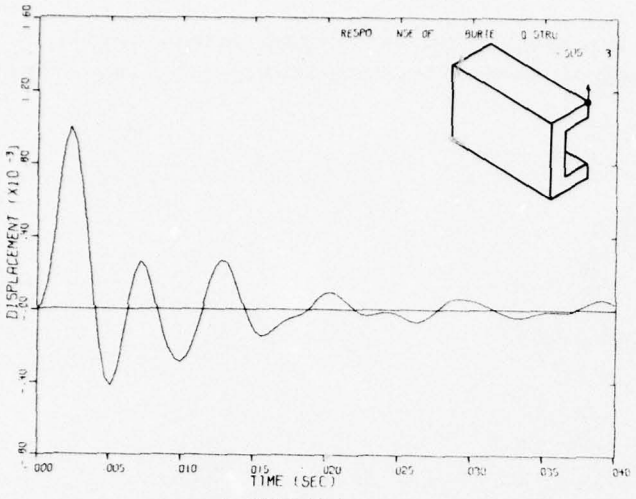
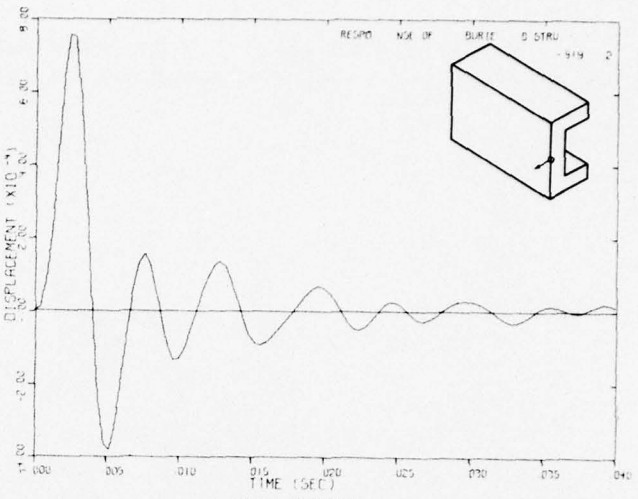


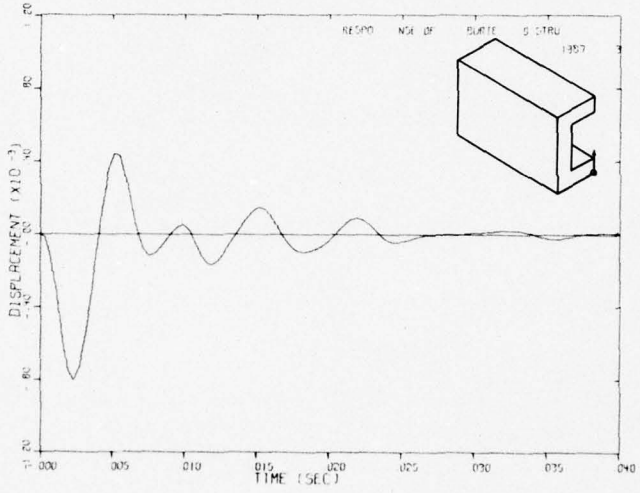
Figure 2-9. Displacement-Time Histories at Various Points on Rectangular Structure Subjected to Loading as Shown in Figure 2-6, Case 1 (Soft Backfill).



a. Midpoint of Roof



b. Midpoint of Sidewall



c. Midpoint of Floor

Figure 2-10. Displacement-Time Histories at Various Points on Rectangular Structure Subjected to Loading as Shown in Figure 2-6, Case 2 (Stiff Backfill).

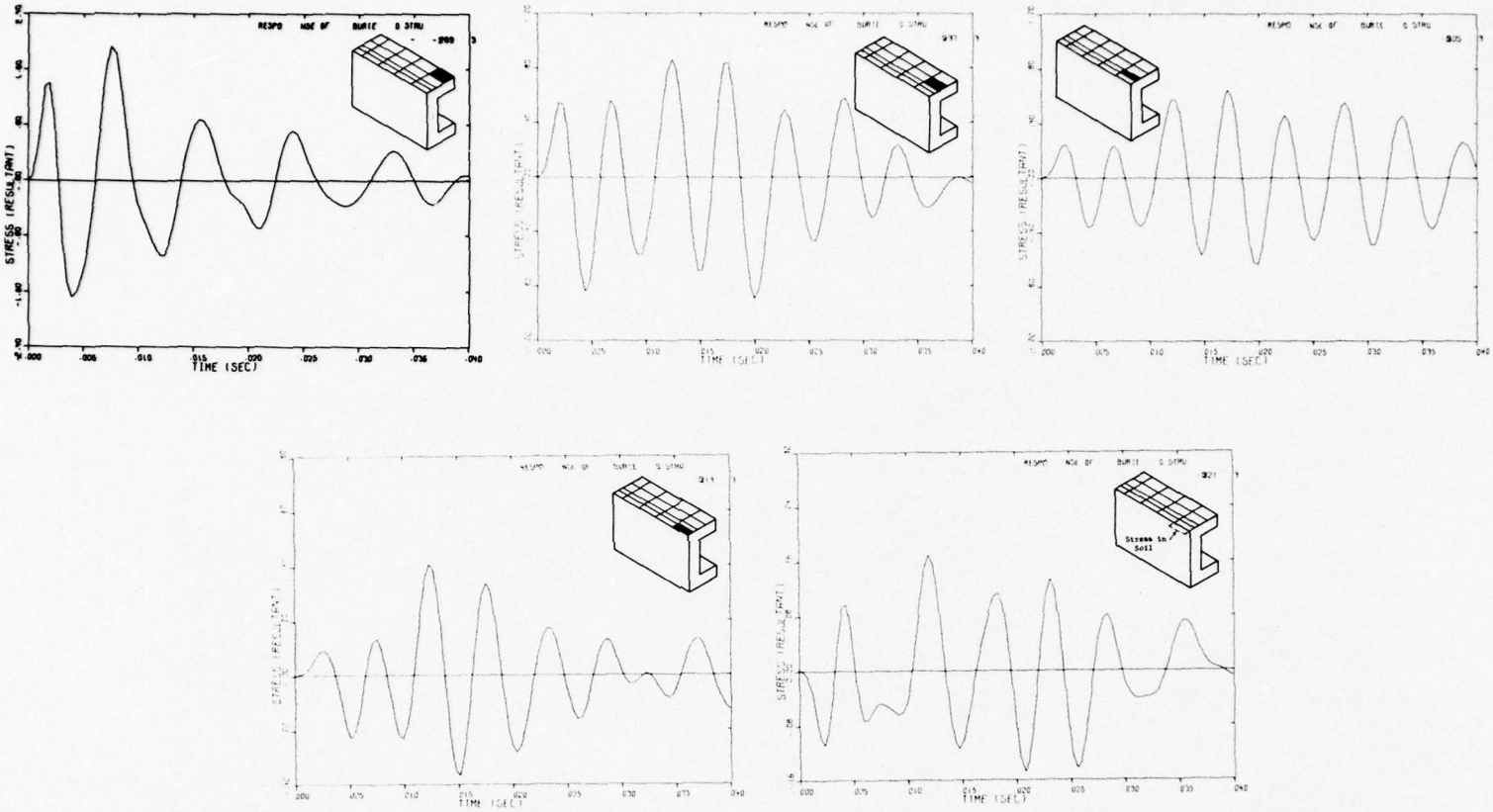


Figure 2-11. Vertical Stress-Time Histories at Soil-Structure Interface Above and Adjacent to Transverse Centerline of Rectangular Structure, Case 1 (Soft Backfill).

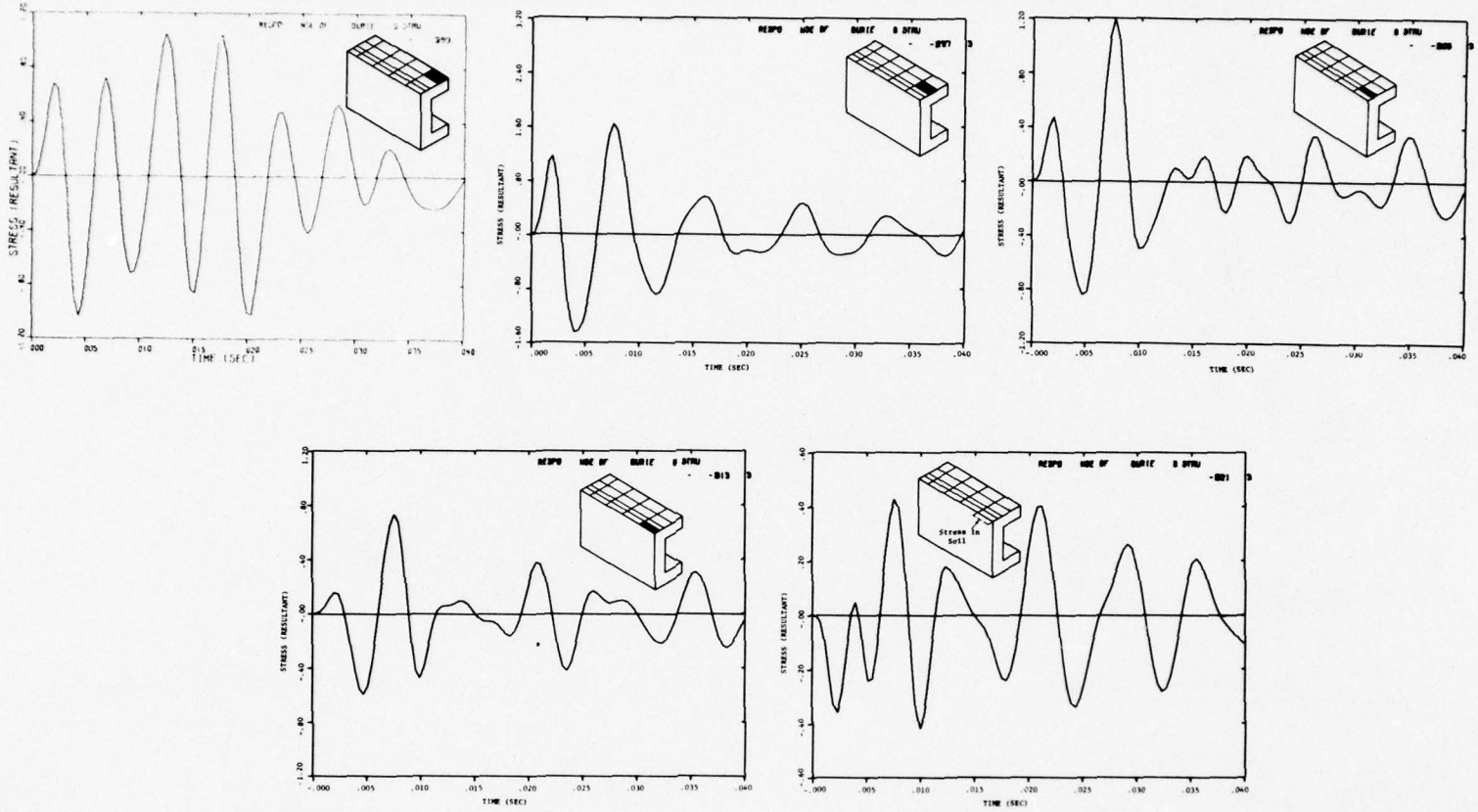


Figure 2-12. Vertical Stress-Time Histories at Soil-Structure Interface Above and Adjacent to Transverse Centerline of Rectangular Structure, Case 2 (Stiff Backfill).

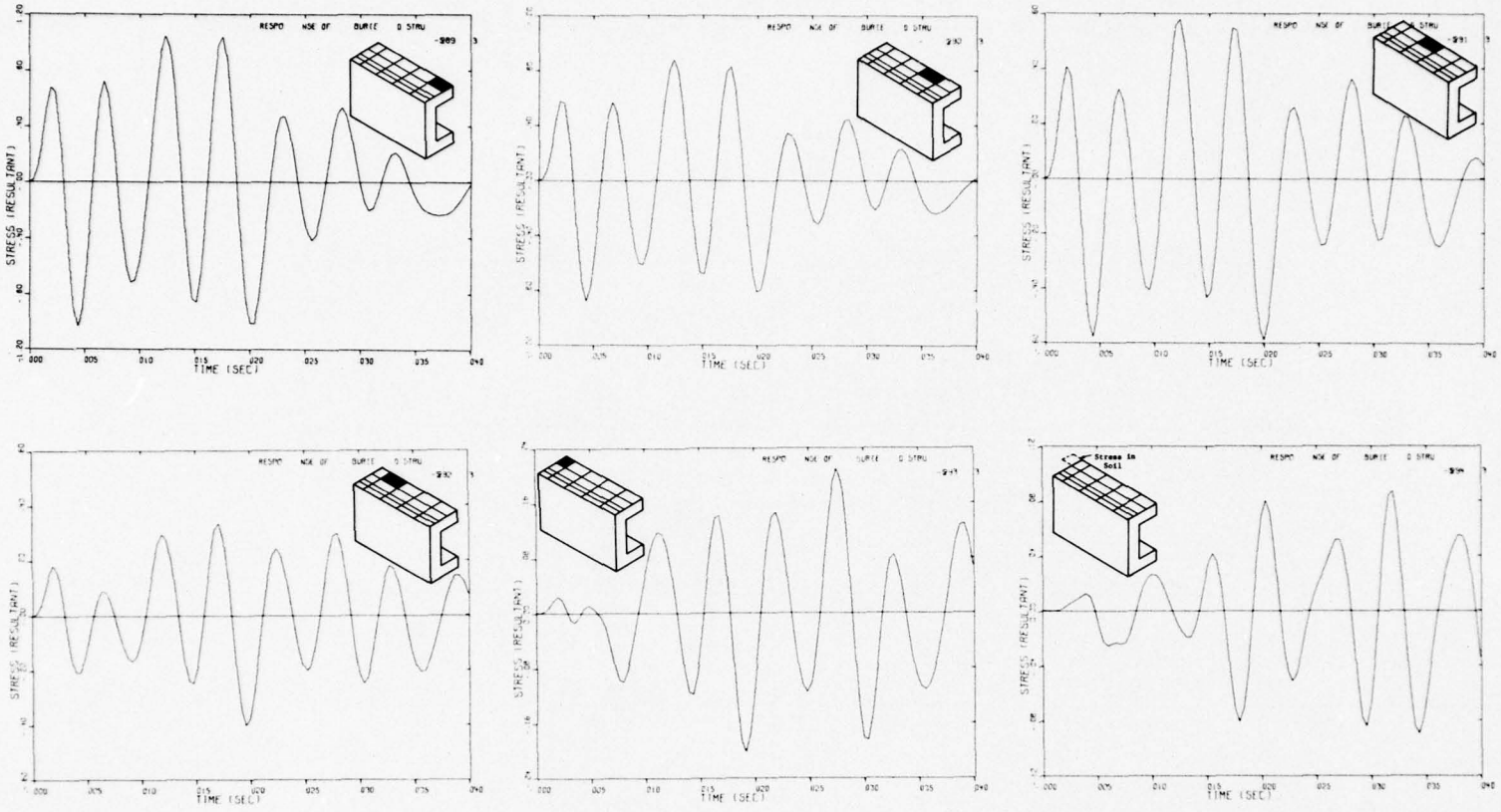


Figure 2-13. Vertical Stress-Time Histories at Soil-Structure Interface Above and Adjacent to Longitudinal Centerline of Rectangular Structure, Case 1 (Soft Backfill).

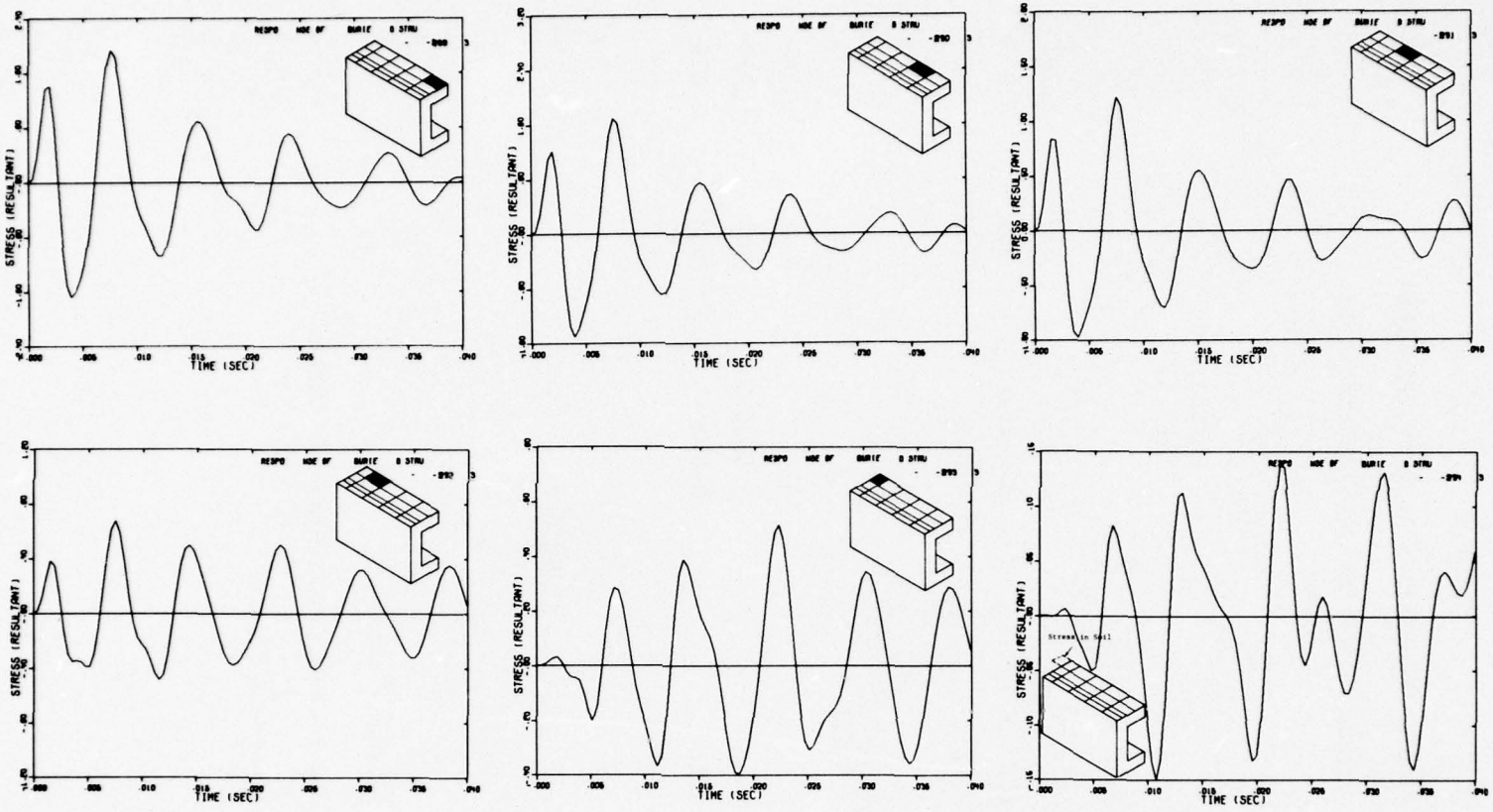


Figure 2-14. Vertical Stress-Time Histories at Soil-Structure Interface Above and Adjacent to Longitudinal Centerline of Rectangular Structure, Case 2 (Stiff Backfill).

TABLE 2-1

MATERIAL PROPERTIES USED IN TRANSIENT

ANALYSIS OF RECTANGULAR STRUCTURE

SOIL

Case	Depth (ft.)	c_s fps	c_p fps
1--Initial Tangent Moduli			
Layer 1	0-3.5	659	1,296
Layer 2	3.5-10.8	983	1,953
Backfill	0-8.2	311	538
2--2X Initial Tangent Moduli (Backfill Only)			
Layer 1	0-3.5	659	1,296
Layer 2	3.5-10.8	983	1,953
Backfill	0-8.2	622	1,076

STRUCTURE

$E = 3.8 \times 10^6$ psi

$\nu = 0.18$

$\rho = 0.000225$ lb.-sec.^{2}/in.^{4}

Roof, floor and sidewall thickness--11 inches

Endwall thickness--16 inches

TABLE 2-2

CALCULATED AND MEASURED FREQUENCIES OF

RECTANGULAR STRUCTURE 3D ($\ell/h = 4$)

UNCOVERED

Mode	Measured Frequency (Hz)	Mode	Calculated Frequency (Hz)
		1	112
1	237	2	214
		3	235
2	310*	4	333
		5	353
3	415		
4	465*		
5	470		
6	521		
7	550*		
8	660*		
9	790		

*Antisymmetrical Mode--Not Calculated by Model with Two Planes of Symmetry

TABLE 2-2 (CONTINUED)

COVERED

Mode	Measured Frequency (Hz)	Mode	Calculated Frequency (Hz)
		1	88
		2	172
1	237	3	180
		4	271
		5	293
2	310*		
3	415		
4	465*		
5	470		

*Antisymmetrical Mode--Not Calculated by Model with Two Planes of Symmetry

TABLE 2-3

FRACTION OF CRITICAL VISCOUS DAMPING FROM CALCULATIONS OF FREE VIBRATION OF BURIED RECTANGULAR STRUCTURE ($\ell/h = 4$)

Case	Cycle 1			Cycle 2			
P-wave speeds based on	Roof	Floor	Side	Roof	Floor	Side	Average
1--Initial Tangent Moduli	0.15	0.13	0.15	0.16	0.13	0.17	0.15
2--Initial Tangent 2 X Moduli	0.21	0.29	0.24	0.06	0.33	0.16	0.22

SECTION 3

NONLINEAR, SINGLE-DEGREE-OF-FREEDOM MODEL OF ROOF SLAB

3.1. INTRODUCTION

The studies described in Section 2 provide estimates of damping parameters to be incorporated in nonlinear single-degree-of-freedom (SDOF) models of the type used in targeting analyses. In order to demonstrate the significance of including reasonable amounts of damping, an existing procedure for analyzing slabs by means of SDOF models was adapted and parameter studies were performed for an airblast loading from a HEST test. This section describes the resistance functions and transformation relationships for the SDOF model and the results of the parameter study. Comparison is made between the response of this model and measurements from a HEST test on structure 3B ($\ell/h = 10$). Response of structure 3D ($\ell/h = 4$) to hypothetical airblast loading is also obtained.

3.2. EQUIVALENT MASS, STIFFNESS AND LOADS FOR SDOF MODEL OF SLAB

The chief failure mechanism for shallow-buried rectangular structures subjected to airblast loading is collapse of the roof. Hence the vulnerability of the structure is assessed by reducing it to a slab having the same dimensions as the physical roof. This slab is then converted to an equivalent SDOF model. The static pressure-deflection relationship is developed from yield line theory for reinforced concrete slabs. The assumed yield line patterns are shown in Figure 3-1. A typical resistance function is illustrated in Figure 3-2. It is divided into several regimes, depending on the state of cracking in the concrete and yielding in the steel. The expressions for the various threshold levels of equivalent concentrated load and displacement constitute the static resistance function for the slab. In the present study, the resistance functions for elastic, elastic-cracked, elastic-plastic and plastic regimes were adopted from Reference 3. A correction for membrane effects was also included when the deflection exceeded the thickness of the slab.

The distributed mass, loading and static resistance of the slab are converted into equivalent discrete quantities for use in dynamic analyses by means

of transformation factors. These take into account the elastic deformed shape and the changes which occur as plastic hinges form. Transformation factors were adopted from Reference 5. Favorable agreement was obtained with models based on simpler transformation factors (Reference 6); hence it appears the results are insensitive to minor changes in these factors.

The equation of motion for the nonlinear SDOF model is written as follows:

$$\underset{\sim}{m}\ddot{\underset{\sim}{x}} = \underset{\sim}{P} + \underset{\sim}{F} \qquad (3\text{-}1)$$

where

$\underset{\sim}{m}$, $F(t)$ = equivalent mass, external force, respectively

$\underset{\sim}{P}$ = internal resisting force. For undamped systems, $\underset{\sim}{P}$ is uniquely a function of $\underset{\sim}{x}$, $p(\underset{\sim}{x})$. For damped systems $\underset{\sim}{p} = p(\underset{\sim}{x}) + c\dot{\underset{\sim}{x}}$

$\underset{\sim}{x}$, $\dot{\underset{\sim}{x}}$, $\ddot{\underset{\sim}{x}}$ = displacement, velocity, acceleration of SDOF model; also correspond to similar quantities at midpoint of span of physical structure

In the computer program used in the present study, the equation of motion is integrated using a fourth order Runge-Kutta technique.

The idealized resistance functions overlook the effect on membrane forces of earth pressure exerted on the walls. Also, the transformation factors for the load do not account for soil arching. Further unresolved questions are what is the effective span, whether the support conditions for the roof slab should be assumed to be fixed or simply supported, and whether shear failure is adequately accounted for in the resistance functions and the transformation factors. It is not the purpose of the present study to try to overcome any of these shortcomings, but exclusively to study the effects of including or omitting damping. Hence, the modeling approach described above is adopted; the results of parametric studies using various amounts of damping for the roof slabs of rectangular structures 3B and 3D are reported below.

3.3. NONLINEAR SDOF ANALYSES OF ROOF SLABS

The effect of damping on SDOF models was investigated by varying damping

ratio as a parameter for given loading conditions and comparing the resulting displacement-time histories. Two loading conditions are considered which are based on measurements in the August 1977 Fort Polk, Louisiana, HEST test on structure 3B. One is the pressure-time history in the HEST cavity, shown in Figure 3-3, and the other is the normal stress exerted on the roof at the center span, shown in Figure 3-4. The former represents a reasonable upper bound on impulse. The latter includes effects of significant arching and as such represents a reasonable lower bound on impulse. These loading functions are applied to models of both structures 3B and 3D, even though only structure 3B has been tested. It is probable the arching which was observed in structure 3B would be different in structure 3D so it may not be typical of a field test situation to use the loads measured on structure 3B for analysis of structure 3D. Further, stress on the roof of structure 3B probably varies in a way which was not detected because there were only three soil-roof interface gages. These difficulties could be overcome with some elaborate models and more measurements, but the objectives of the present project require that the simplest models be used and this is what is done.

The displacement-time histories for the SDOF model of roof of structure 3B (clamped edges) subjected to loading based on interface pressure are shown in Figure 3-5. Four damping ratios corresponding to 0, 10 percent, 15 percent and 20 percent of critical were considered, which nearly covers the range of damping ratios calculated in the previous study on the arch, Reference 1, and the present study on structure 3D. The damping coefficient in the SDOF model is calculated on the basis of the following expression:

$$c = \eta \ (2\sqrt{km}) \qquad (3\text{-}2)$$

where

k = stiffness of the elastic-plastic regime of the SDOF model
m = mass of the SDOF model
η = fraction of critical damping

As Figure 3-5 shows, there is a major effect when the viscous damping equal to 10 percent of critical is included; the effect increases moderately when the damping is increased to 20 percent of critical. The total effect for 20 percent damping is to reduce maximum displacement to about 40 percent of that in

the undamped case. Threshold values of displacement which separate the various regimes of behavior such as elastic-cracked, elastic-plastic and fully plastic are indicated.

The computed displacement-time history cannot be compared with data because no measurements of transient roof sag were made. However, a permanent deflection or roof sag of 0.5 in. was measured by surveying after the test and it is tempting to try to compare this aspect of the data with the calculation. There is considerable uncertainty in defining the unloading branch of the resistance function. As is shown in Figure 3-2, the elastic-plastic and elastic-cracked slopes are reasonable lower and upper bounds, respectively, on the unloading slope; as the figure suggests, the uncertainty in these slopes can lead to a large uncertainty in permanent roof deflection. These unloading slopes were applied in the 20 percent damping case considered in Figure 3-5 (structure 3B, interface pressure-time history loading). The corresponding resistance-deflection path is shown in Figure 3-6. If unloading is assumed to be governed by the elastic-plastic slope, the calculated permanent displacement would be 0.24 in.; if unloading is assumed to be governed by the elastic-cracked slope, the calculated permanent displacement would be 0.74 in. These values bound the measured value of 0.5 in.

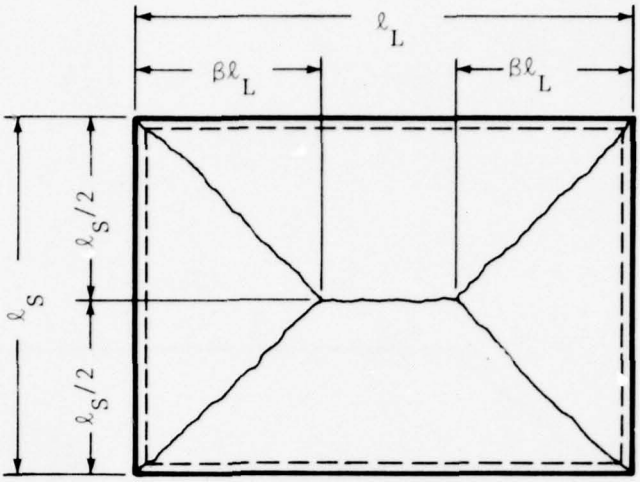
Results of the analysis of structure 3B, with loading based on pressure in the HEST cavity, are shown in Figure 3-7 for two assumed values of critical viscous damping. There is much more impulse in this loading function than in the one based on interface pressure and hence the calculated sag is much greater. Since the absolute velocities are higher in the case with HEST cavity pressure input, the damping contribution to F, Equation (3-1), is also significantly greater. Thus the reduction in roof sag due to increasing damping from 10 percent to 20 percent of critical is greater in this case than in the one based on interface pressure loading.

Similar results were obtained for the model of structure 3D when it was subjected to the same loads. Results for the loading based on interface stress measurements made during a test of structure 3B (and hence not necessarily applicable to structure 3D) are shown in Figure 3-8. The velocities, displacements and effect of including damping are significantly less for structure 3D than for

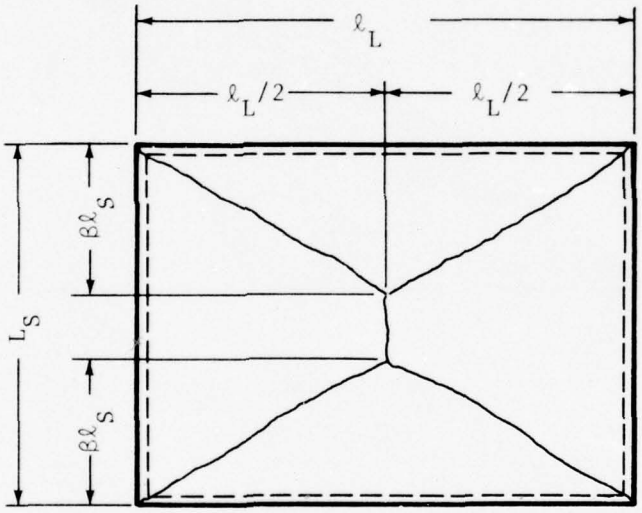
structure 3B. This is to be expected since structure 3D is much stiffer and stronger than structure 3B. As before, greater roof sag and greater effect of including damping is observed when the HEST cavity pressure is used as input, Figure 3-9.

The interpretation of these findings is complicated by the significant uncertainties involved in transforming a physical structure into a SDOF model. These include the effective span, the edge support conditions, the applicability of yield line theory and how to incorporate arching effects. There is also uncertainty concerning the fundamental step of representing radiation damping in the physical structure by a constant percentage of critical viscous damping based on the elastic-plastic stiffness.

In spite of these uncertainties, the examples described above indicate clearly that even such light damping as 10 percent of critical significantly reduces the response calculated by SDOF models.



a. Collapse Mode "a"



b. Collapse Mode "b"

NOTATION: ——— Positive Yield Line
– – – – Negative Yield Line

Figure 3-1. Assumed Collapse Modes (Yield Lines) for Reinforced Concrete Slab.

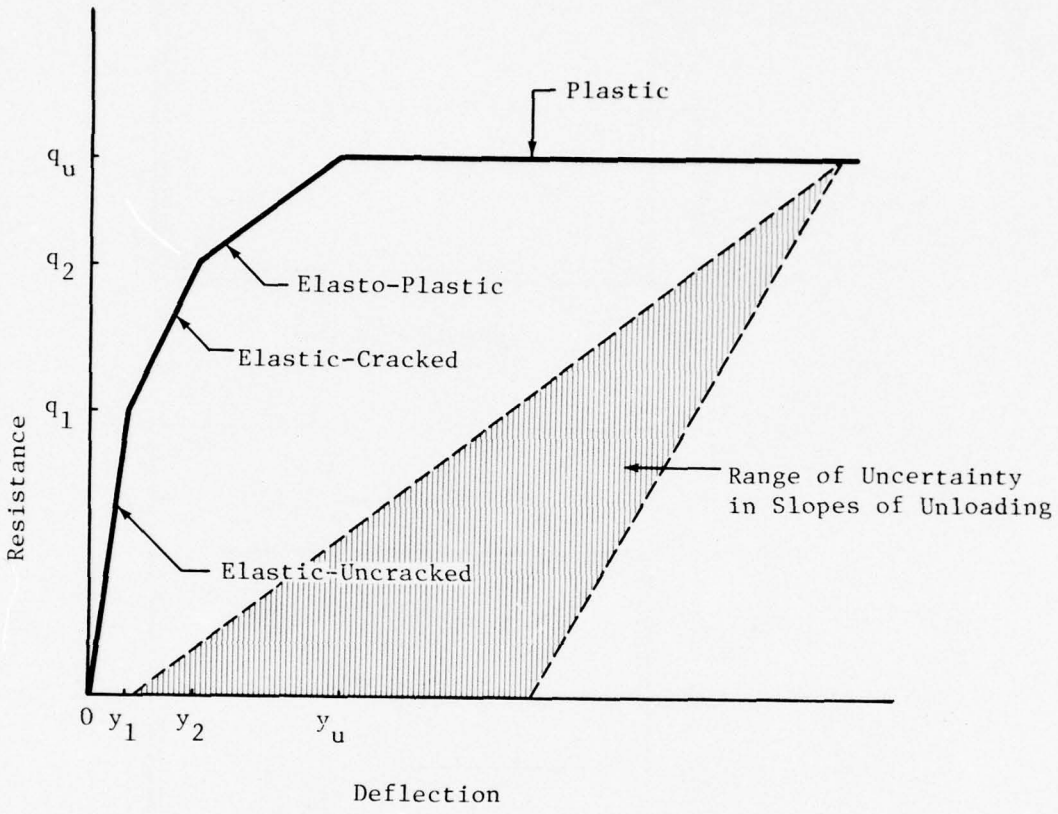


Figure 3-2. Resistance Function for a Reinforced Concrete Slab.



Figure 3-3. Airblast Overpressure Measured in HEST Cavity. HEST Test on Structure 3B, August 1977.

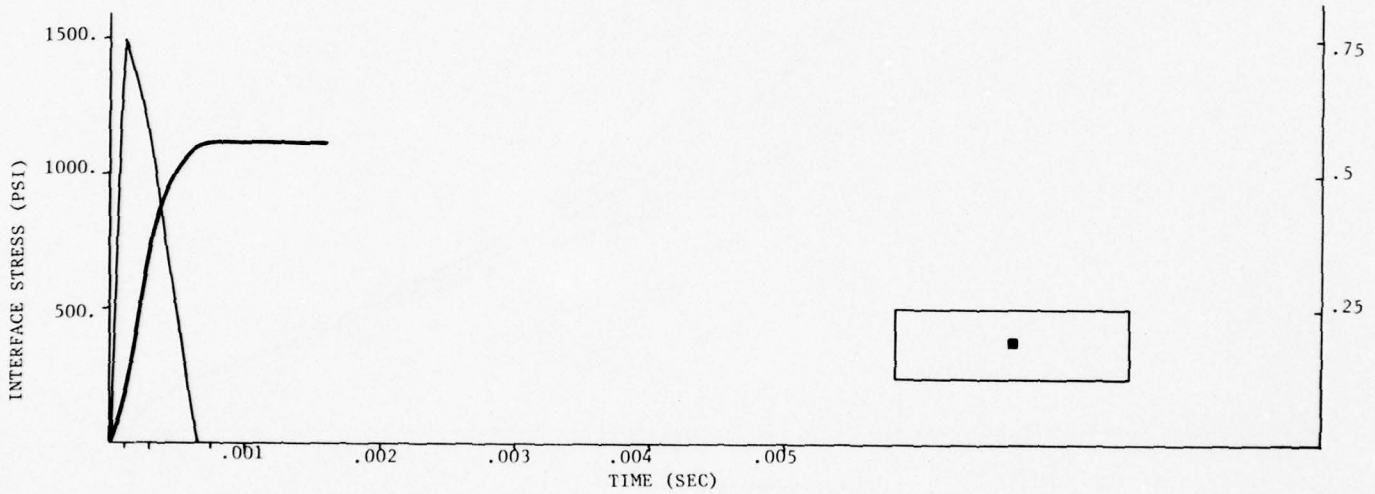


Figure 3-4. Interface Stress Exerted by Soil on Roof of Structure 3B. HEST test on Structure 3B, August 1977.

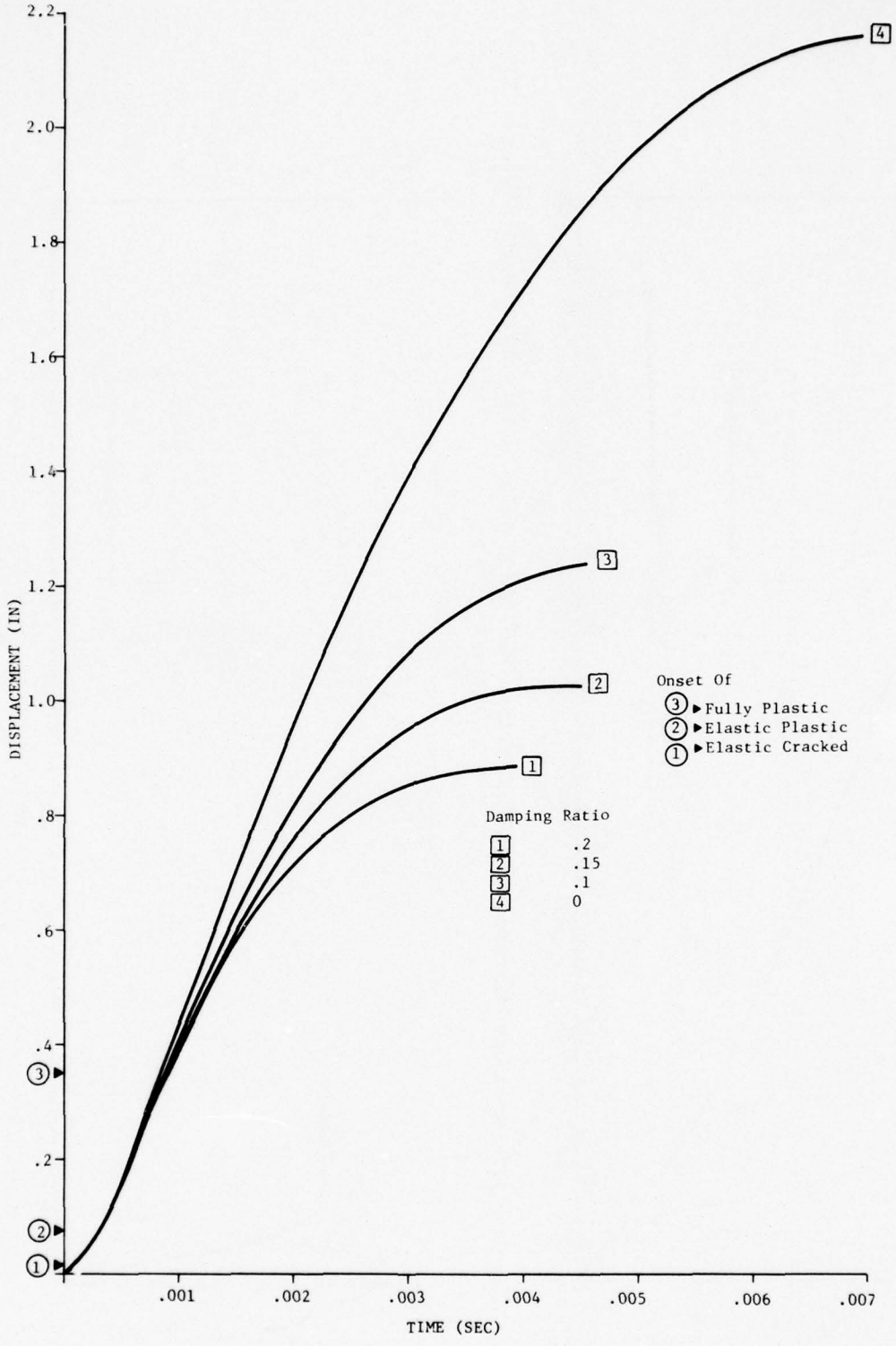


Figure 3-5. Displacement-Time History for SDOF Model (4 Different Damping Ratios) and for Midpoint of Roof for Structure 3B ($\ell/h = 10$) Subjected to Measured Interface Stress-Time History.

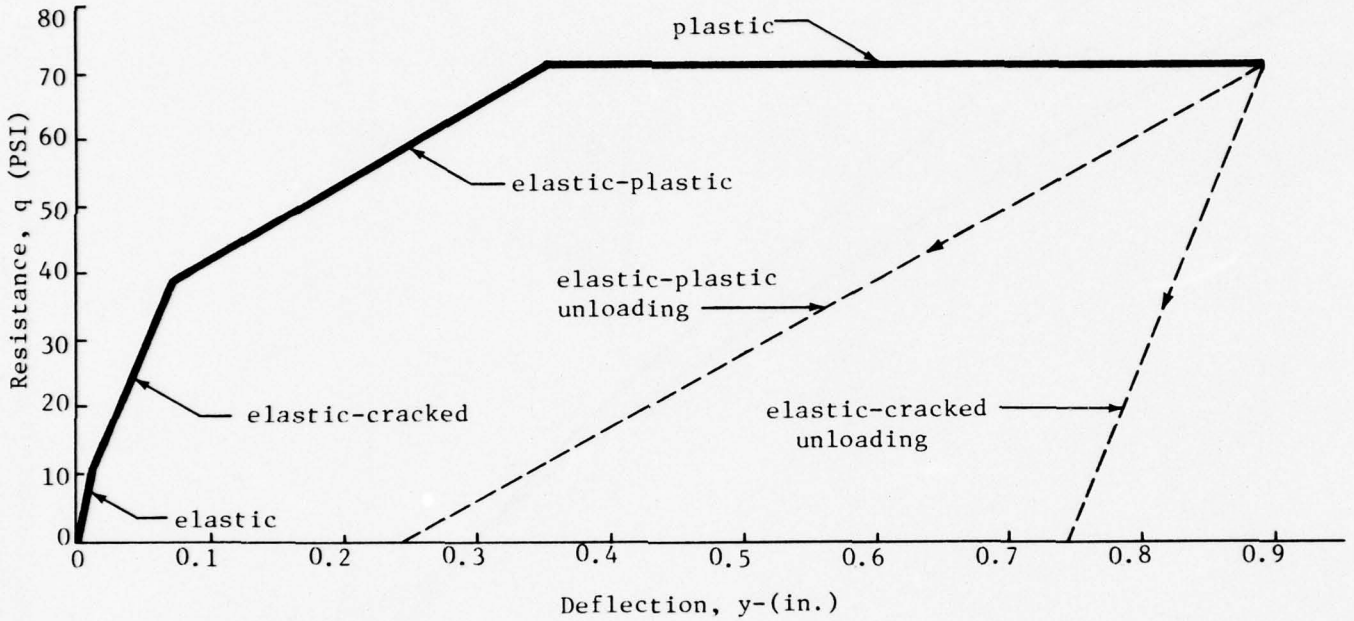


Figure 3-6. Resistance-Deflection Function; Also Path for SDOF Model of Structure 3B, Including 20 Percent Critical Damping, Subjected to Measured Interface Pressure Loading.

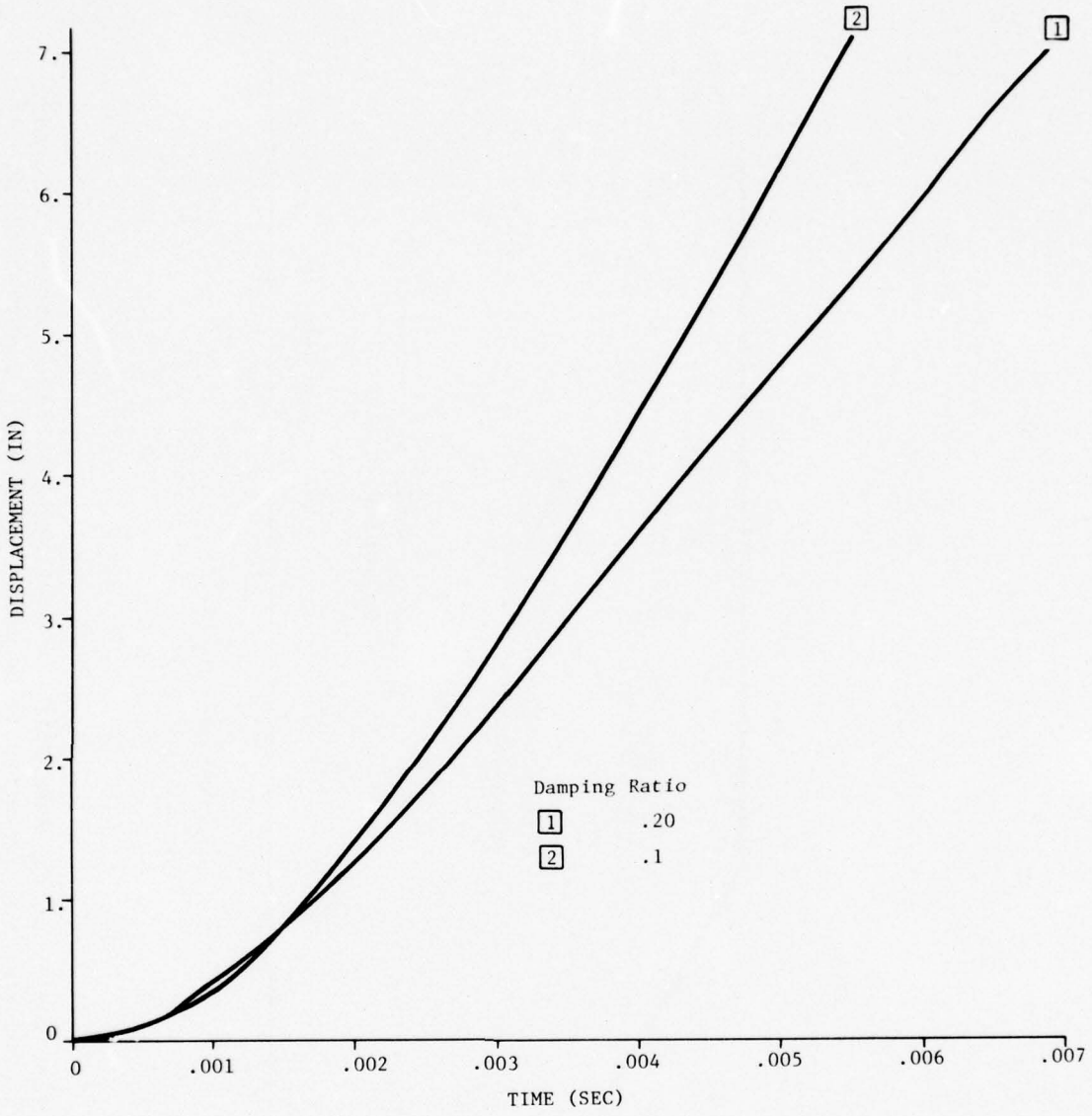


Figure 3-7. Displacement-Time History for Structure 3B (Thin Box ℓ/h = 10) Applied Load Based on HEST Overpressure.

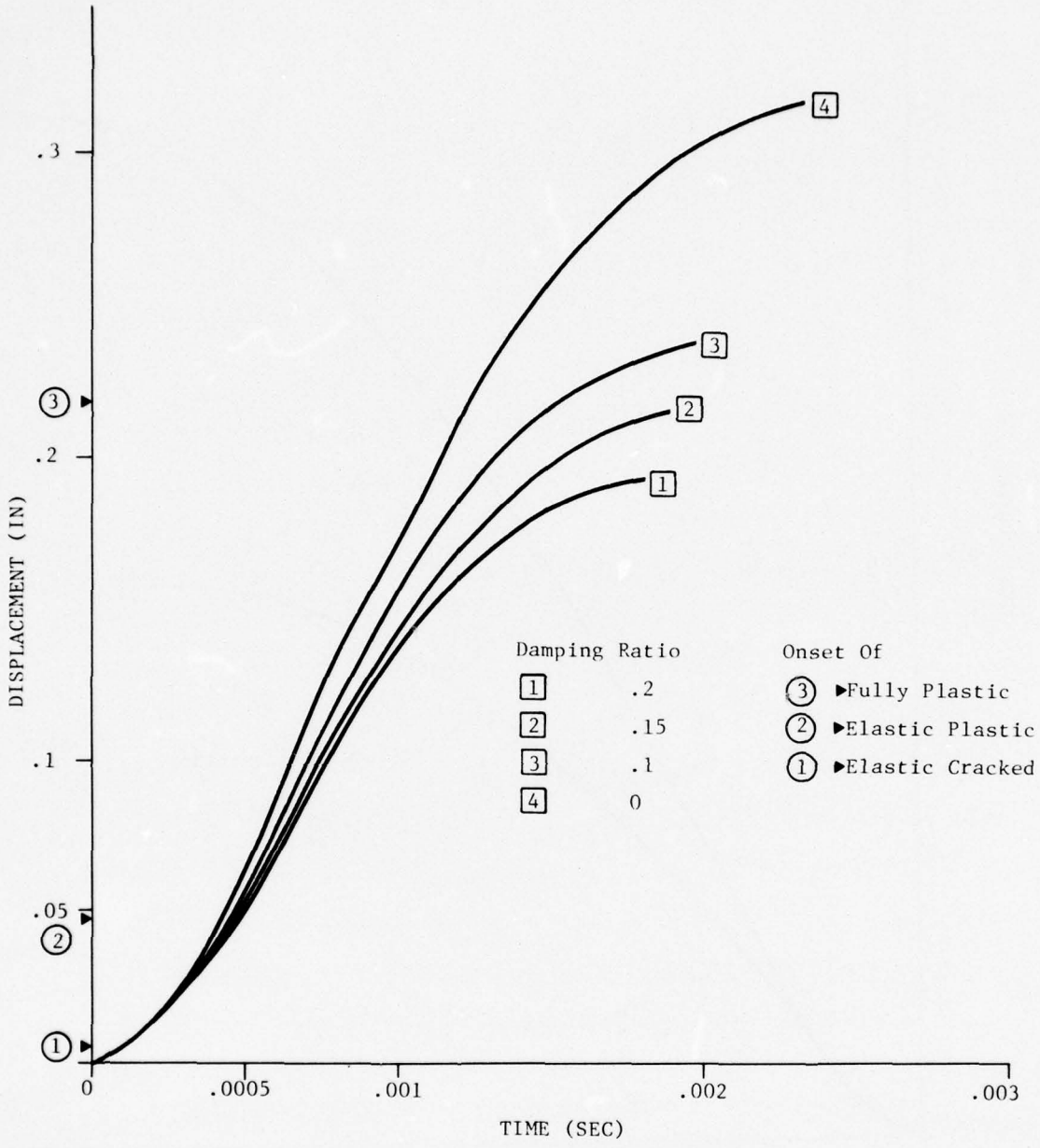


Figure 3-8. Displacement-Time History for Structure 3D (Thick Box ℓ/h = 4) Applied Load Based on Interface Pressure for Structure 3B.

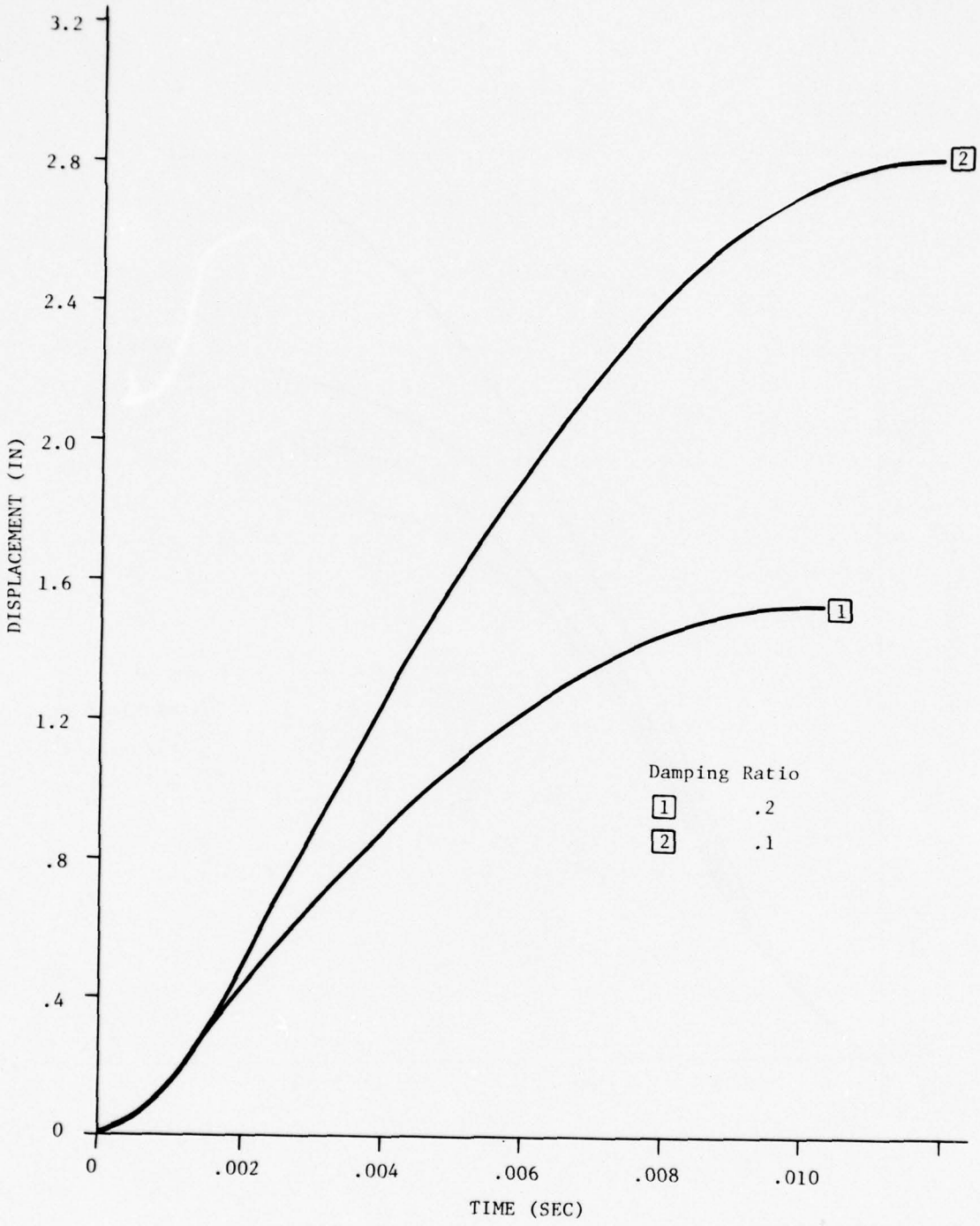


Figure 3-9. Displacement-Time History for Structure 3D (Thick Box ℓ/4 = 4.4) Applied Load Based on HEST Overpressure.

SECTION 4

SCALING RULES FOR RADIATION DAMPING ASSOCIATED WITH VIBRATIONS OF A CYLINDRICAL CAVITY

The equations governing frequency and radiation damping characteristics for a cylindrical structure embedded in an infinite medium have been formulated so that basic relationships among wave speed and frequency can be understood for each mode. Such relationships provide insight into how to scale or extrapolate knowledge of radiation damping gained from specific finite element anlyses to new cases involving different geometry and material properties. Scaling rules indicate how frequency, wave speed and size of structures can be varied to increase or decrease radiation damping. For example, if two structures having different frequencies of deformational modes are embedded in identical backfill and soil, it is helpful to know how natural frequencies of the structures are modified and which is more highly damped. Moreover, if radiation damping associated with one of the structures is known, scaling rules may suggest how to estimate radiation damping for the other. Cylindrical geometry is adopted because it is the closest simple approximation to a plane section perpendicular to the long axis of the rectangular and arch structures considered in the present and previous analyses. The work described below assumes that the relationships which apply to the cylinder also apply qualitatively to more complicated geometry and material properties such as a rectangular structure or an arch embedded in backfill with nonlinear properties. Further field and laboratory testing and possibly computations are needed to confirm this assumption.

The following analysis involves coupling a cylindrical shell, represented by its flexural modes, to a cylindrical cavity in an infinite elastic domain. The coupled equations of motion are expressed in terms of a frequency equation for each mode shape (rigid body, $n = 1$, ovaling, $n = 2$, etc.). The solution is restricted to lower modes ($n < 5$) where coupling between flexural and extensional modes can be neglected, Reference 7. The frequency equation has several roots for each mode shape, corresponding to the multiple frequencies and damping for modes of the cavity. The dominant mode can be selected by evaluating and comparing the participation factors for each solution. The present study carries the

solution to the point of examining the response in each mode, including frequency characteristics and damping. Synthesis of the modes could be performed to obtain a complete dynamic solution, Reference 7, but this is not our goal. The overall solution to this problem, which is given below, is not new. A form of the solution, using doubly asymptotic methods, is available in Reference 8 and was used in evaluating the effects of embedment on frequencies and damping ratios of a cylinder in Reference 1. However, Reference 8 is not intended for this purpose; a more convenient solution is given below in the form of a chart which is intended to be used by targeting analysts.

4.1. THEORETICAL DEVELOPMENT

Consider a thin-walled elastic cylindrical shell with circular cross section, embedded in an elastic continuum as shown in Figure 4-1. Assume that the shell and continuum are in welded contact and that a state of plane strain exists. Further assume that any free surface or material discontinuity is far from the cylinder and that the shell deformation is due primarily to in-plane flexure (in contrast to membrane extension). Under these assumptions modal response of the embedded cylinder can be described by one generalized coordinate, $q_n(t)$, as (Reference 9),

$$w = q_n(t) \cos n\theta, \tag{4-1a}$$

$$v = \frac{q_n(t)}{n} \sin n\theta, \tag{4-1b}$$

where w is the radial displacement, positive inward and v is the tangential displacement positive in the direction of increasing θ (counterclockwise).

At $t = 0$ the n^{th} flexural mode is impulsively excited by a suitable force distribution varying like a delta function in time. The response is composed of damped harmonic oscillations (damping due to radiated elastic energy) and rapidly decaying starting transients (not examined further). We wish to find the damped frequency and damping ratio of the modes of such a system as a function of cylinder and continuum properties.

The solution is found by writing the single-degree-of-freedom equation of motion for the cylinder subject to reactive forces from the surround-

ing continuum. Ignoring starting transients we look for solutions of the form

$$q_n(t) = u_n e^{-i\omega t}$$

Substituting into the governing differential equation gives the frequency equation, a numerical solution of which yields the admissable complex frequencies, ω. The imaginary part of ω is due to components of the reactive force on the shell in phase with the shell velocity.

The governing shell equation is derived via the Euler-Lagrange formulation. The kinetic and potential anergies, T and V, for lower modes of the vibrating cylinder are:

$$T = \frac{1}{2}\pi\rho' ah\left(1 + \frac{1}{n^2}\right)\dot{q}_n^{\,2} = \frac{1}{2} m_n \dot{q}_n^{\,2}, \qquad (4\text{-}2a)$$

$$V = \frac{1}{2}\frac{\pi}{12}\left(\frac{h}{a}\right)^3 \frac{E'}{1 - G'^2}(n^2 - 1)^2 q_n^{\,2} = \frac{1}{2} k_n q_n^{\,2}, \qquad (4\text{-}2b)$$

where m_n and k_n are the modal mass and stiffness, respectively and prime ($'$) quantities refer to the properties of the shell. Substituting into the Euler-Lagrange differential equation,

$$\frac{d}{dt}\left(\frac{\partial T}{\partial \dot{q}_n}\right) + \frac{\partial V}{\partial q_n} = F_n \ , \qquad (4\text{-}3)$$

and dividing by m_n yields

$$\ddot{q}_n + \omega_n^{\,2} q_n = \frac{F_n}{m_n} \ , \qquad (4\text{-}4)$$

where F_n is the generalized force due to radiation, and $\omega_n^{\,2} = k_n/m_n$ is the in vacuo natural frequency of the cylinder.

To evaluate the generalized force of the continuum on the cylinder, the stresses are calculated on the surface of a cavity subject to the cylinder displacements (see Figure 4-2). Outward propagating waves from a driven cavity are found in terms of displacement potentials Φ and Ψ (Reference 10) as

$$\Phi = e^{-i\omega t} A_n H_n(K_p r)\cos n\theta\,; \qquad K_p \equiv \omega/c_p \ , \qquad (4\text{-}5a)$$

$$\Psi = e^{-i\omega t} B_n H_n(K_s r)\sin n\theta\,; \qquad K_s \equiv \omega/c_s \ , \qquad (4\text{-}5b)$$

where A_n and B_n are complex constants, H_n is the Hankel function of the first kind, K_p, K_s are wave numbers related to the frequency as shown, and c_p and c_s are the dilatational and shear wave speeds, respectively. Substituting these solutions into the displacement-potential relations,

$$u_r = \Phi_r + \frac{1}{r} \Psi_\theta, \tag{4-6a}$$

$$u_\theta = \frac{1}{r} \Phi_\theta - \Psi_r, \tag{4-6b}$$

applying the prescribed cavity displacement, Equation (4-1) with $q_n = u_n e^{-i\omega t}$, yields expression for A_n and B_n as functions of frequency. Finally, substituting the potentials into the stress-potential relations

$$\sigma_{rr} = \frac{\lambda}{c_p^2} \Phi_{tt} + 2G' \left(\Phi_{rr} - \frac{1}{r^2} \Psi_\theta + \frac{1}{r} \Psi_{r\theta}\right), \tag{4-7a}$$

$$\sigma_{r\theta} = 2G' \left(\frac{1}{2c_s^2} \Psi_{tt} - \Psi_{rr} + \frac{1}{r} \Phi_{\theta r} - \frac{1}{r^2} \Phi_\theta\right), \tag{4-7b}$$

results in the normal and tangential cavity stresses written as

$$\sigma_{rr} = 2G' C_n(\Omega) \frac{u_n}{a} e^{-i\omega t} \cos n\theta, \tag{4-8a}$$

$$\sigma_{r\theta} = 2G' D_n(\Omega) \frac{u_n}{a} e^{-i\omega t} \sin n\theta, \tag{4-8b}$$

where C_n and D_n are function of the non-dimensionalized frequency defined as

$$\Omega \equiv \frac{a\omega}{c_s}. \tag{4-9}$$

The generalized force, F_n, is found by the method of virtual work. Referring to Figure 4-2 we see that

$$\delta W = F_n \delta q_n = \int_0^{2\pi} (-\sigma_{rr} \delta_w + \sigma_{r\theta} \delta_v) a d\theta, \tag{4-10}$$

hence

$$F_n = 2\pi G' \left(-C_n(\Omega) + \frac{1}{n} D_n(\Omega)\right) q_n \tag{4-11}$$

Substituting F_n into the shell equation, Equation (4-4), and setting $q_n(t) = u_n e^{-i\omega t}$ yields the frequency equation for the cylinder as

$$\Omega^2 - \Omega_n^2 + \frac{4}{M}\frac{n^2}{n^2+1}\left(-C_n(\Omega) + \frac{1}{n}D_n(\Omega)\right) = 0, \tag{4-12}$$

where Ω is the damped natural frequency, Ω_n is the in vacuo natural frequency, given by

$$\Omega^2 \equiv \frac{a^2\omega_n^2}{c_s^2} = \frac{c_o}{c_s}\left(\frac{h^2}{12a^2}\right)\frac{n^2(n^2-1)^2}{n^2+1}, \tag{4-13}$$

with

$$c_o^2 = \frac{E'}{\rho'(1-G'^2)}, \tag{4-14}$$

and

$$M \equiv \frac{2h\rho'}{a\rho} \tag{4-15}$$

is the mass ratio defined as the ratio of cylinder to displaced soil mass per unit length.

Writing solutions of the frequency equation as

$$\Omega = \Omega_d - iB \quad \text{or} \quad \omega = \omega_d - i\beta,$$

then the generalized coordinate, q_n, becomes

$$q_n(t) = u_n e^{-\beta t}(\cos\omega_d t + i\sin\omega_d t). \tag{4-16}$$

Damping is best measured by the damping ratio, η, defined as the ratio of actual to critical damping (when $\frac{\omega_d}{\beta} \to 0$) and given by

$$\eta = \sin\left(\tan^{-1}\frac{\beta}{\omega_d}\right) = -\sin(\mathrm{ARG}(\omega)) \tag{4-17}$$

The change in frequency due to embedment is measured by ζ, the ratio of damped frequency to in vacuo natural frequency

$$\zeta = \omega_d/\omega_n. \tag{4-18}$$

The dynamic response is explicitly dependent on two-dimensionless parameters, namely the in vacuo natural frequency, Ω_n, and the mass ratio, M. The rigid body mode, n = 1, depends on the mass ratio only, while the flexural modes, n = 2, 3, . . ., depend on both. Observe that in the limiting case of a light, flexible shell multiplying the frequency equations by M and letting $M \to 0$ results in

$$-C_n(\Omega) + \frac{1}{n}D_n(\Omega) = 0.$$

The solution, Ω_c, is the frequency of an oscillating, inextensible cavity.

4.2. SOLUTION AND APPLICATION TO CASES OF PRACTICAL INTEREST

Equation (4-12) was solved for the embedded frequency as a function of the in vacuo natural frequency (Equation 4-13) and the mass ratio (Equation 4-15). From the embedded frequency, the frequency (ζ) and damping ratios (η) were calculated (Equations 4-17 and 4-18). Mode 1 (rigid body), Mode 2 (ovaling) and Mode 3 were investigated. Except for very massive structures the n = 1 mode is critically damped, while the n = 3 mode is qualitatively similar to n = 2 but with generally less damping; these modes are not discussed further. Typical results are shown graphically for the n = 2 mode with mass ratios M = 0.1, 0.34 and 1.0. The ratio of c_p to c_s is 2 for these results. The n = 2 mode is chosen because it is the principal mode of deformation at early times for many protective structures. The mass ratios cover the range for practical design of protective structures. For example, the mass ratios for the arch, Reference 1, and for rectangular structure 3B ($\ell/h = 10$) are about M = 0.4; rectangular structure 3D (the subject of Section 2 of the present report) has mass ratio $M \simeq 1.0$.

The solution to Equation 4-13 has multiple roots for each mode shape. This arises from the response of the cavity (not of the shell). The consequence of these multiple roots is multiple frequencies and damping ratios of the coupled soil-structure system. The root which dominates the response in each mode in a particular application depends on the nature of the excitation and the duration of response which is of interest. The roots selected to be shown in this report are those corresponding to results reported in Reference 1 and to the results obtained by the present writers in analyzing the box. The roots may not always dominate.

Figure 4-3a,b show the frequency and damping ratios for the case of the ovaling mode with mass ratios M = 0.34 and 1.0, respectively. The abscissa is the frequency parameter,

$$\Omega_n = \frac{a\omega_n}{c_s}.$$

Increasing the frequency parameter implies larger structure (larger radius, a),

stiffer structure (larger in vacuo frequency, ω_n) or softer soil (smaller shear wave speed, c_s). As Ω_n increases the damping decreases while the frequency approaches the in vacuo value. One interpretation of this is that, as the soil becomes softer, the soil-structure system tends toward the in vacuo case.

Comparison is made in Figure 4-3a with results reported in Reference 1 which were obtained by the Doubly Asymptotic Approximation for the same soil-structure system. Agreement is satisfactory. Comparison is made in Figure 4-3b with results of the present finite element analysis of rectangular structure 3D. This comparison is only approximate because of differences in the shapes of the structures considered in the two analyses; however, ovaling-type mode shapes are exhibited by both structures. Also, in the case of structure 3D there is a free surface, which tends to lower the embedded frequency and decrease radiation damping. In view of these differences the degree of agreement is acceptable.

Figure 4-4 shows the damping ratios for the range of mass factors considered; Figure 4-5 shows the corresponding frequency ratios. This is the same information which is presented in Figure 4-3 with the case M = 0.1 added. These figures can be used in the design and interpretation of tests and calculations for structures whose deformations can be approximated by the ovaling mode of a cylinder. Two practical and significant applications are:

a. A structure and its backfill can be designed to give maximum or minimum response by appropriate choice of the parameter $\Omega_n = \frac{\omega_n a}{c_s}$.

b. Elastic frequency and damping ratios can be estimated for single-degree-of-freedom models.

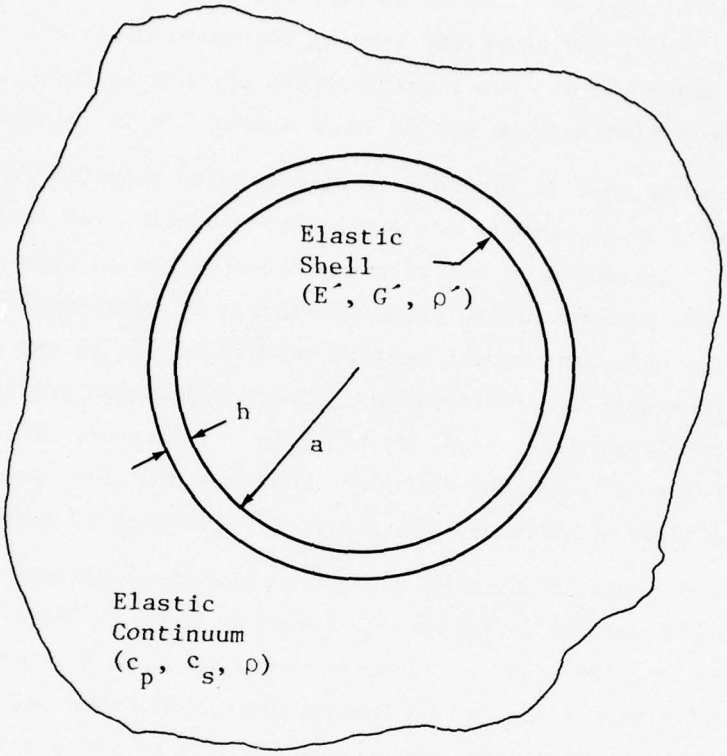
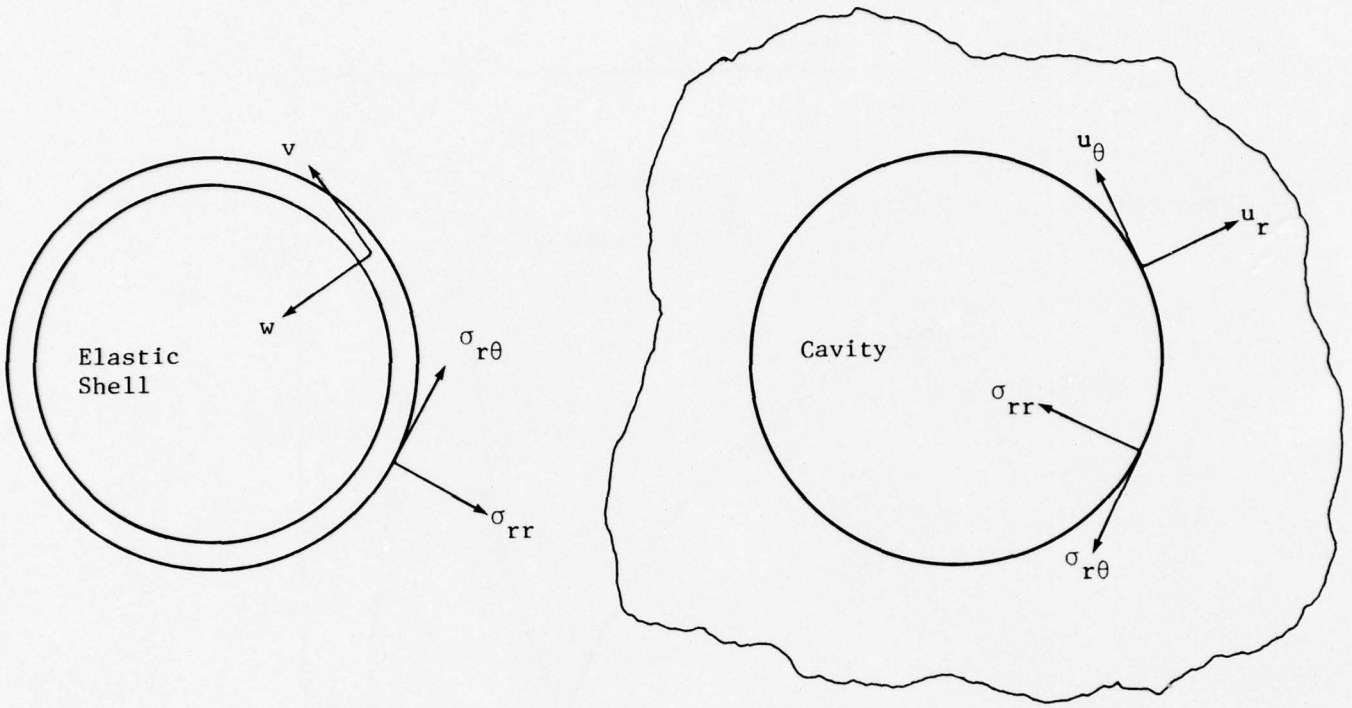


Figure 4-1. Shell Embedded in an Elastic Continuum.



$w = q_n(t) \cos n\theta$

$v = \frac{1}{n} q_n(t) \sin n\theta$

$u_r = - w$

$u_\theta = v$

Figure 4-2. Coupling of Shell and Cavity.

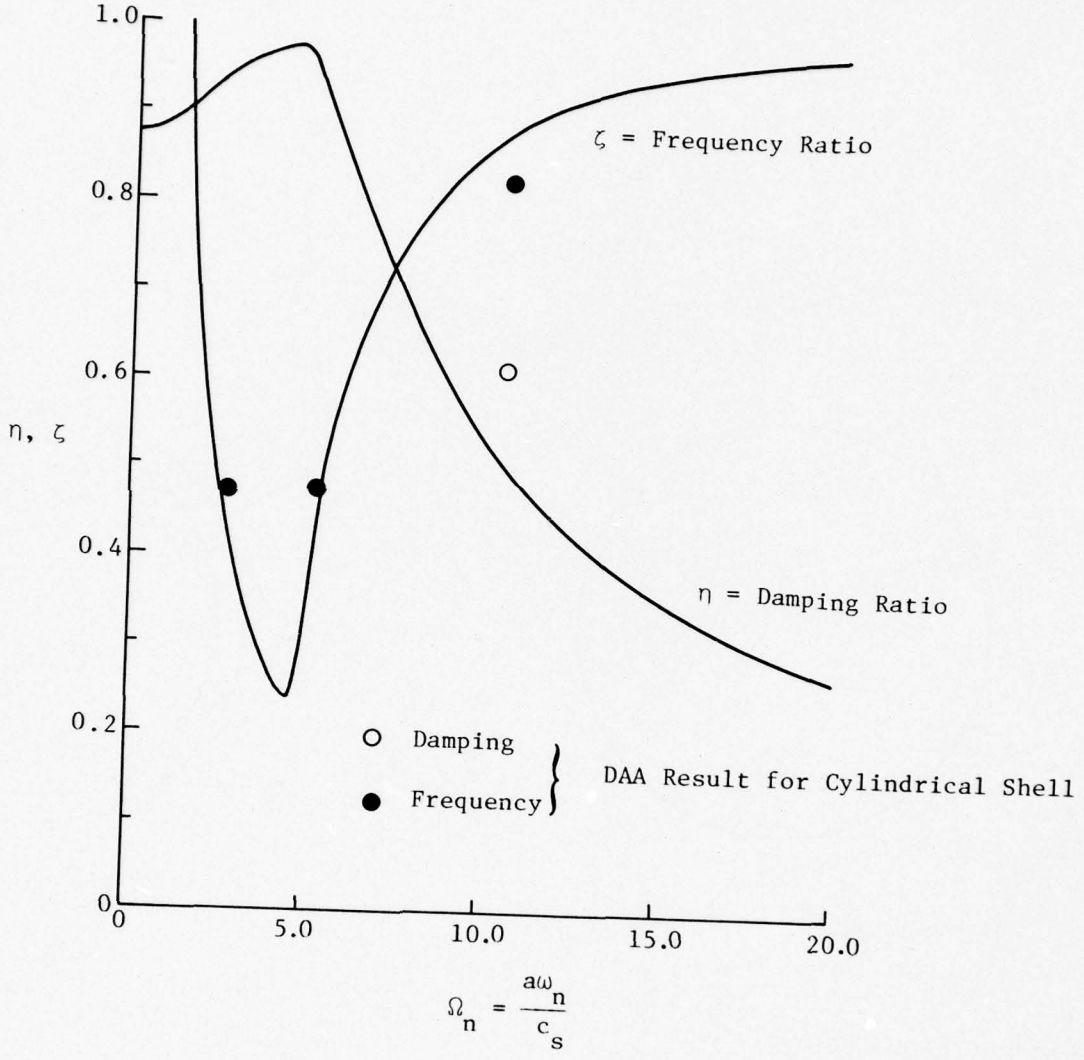


Figure 4-3a. Response of n = 2 Mode, M = 0.34.

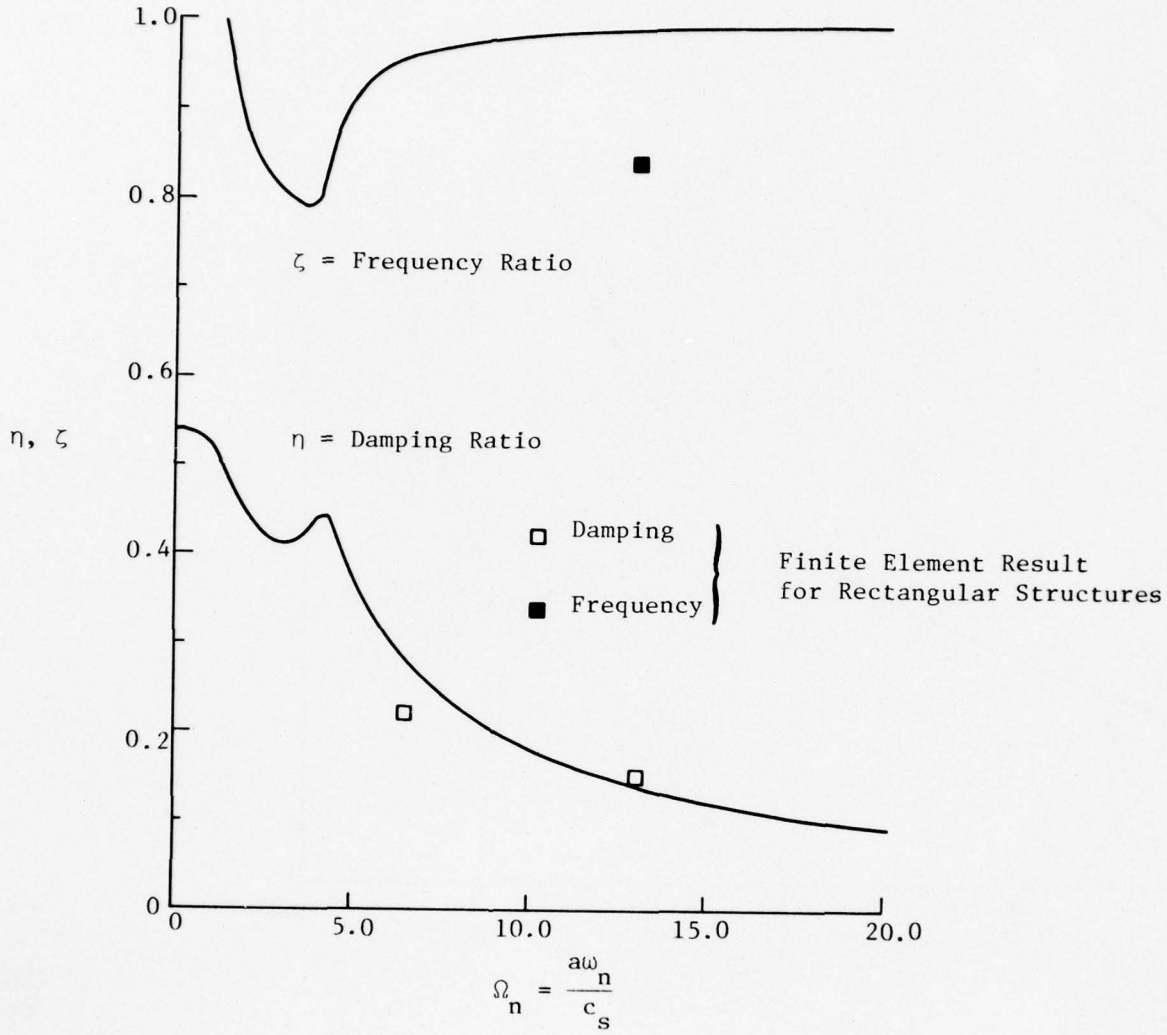


Figure 4-3b. Response of n = 2 Mode, M = 1.0.

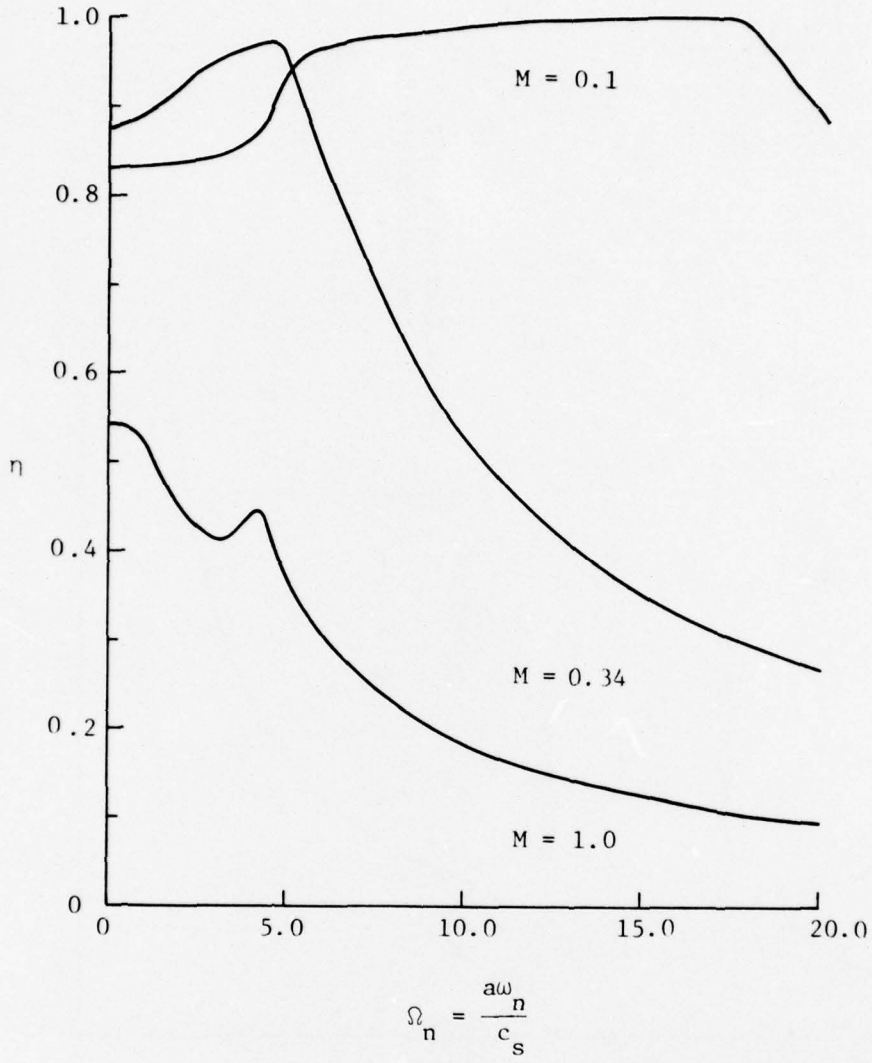


Figure 4-4. Damping Ratio for Various Mass Ratios.

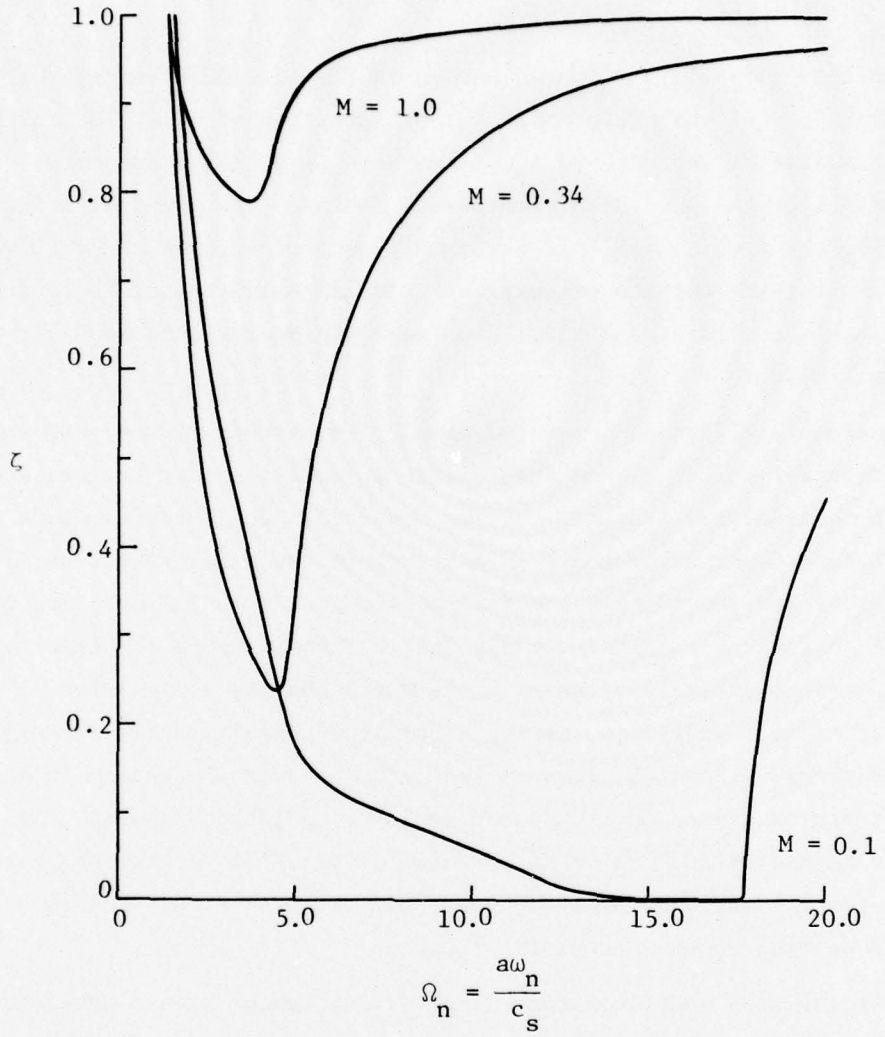


Figure 4-5. Frequency Ratio for Various Mass Ratios.

SECTION 5

SUMMARY AND RECOMMENDATIONS

Modal analysis of covered and uncovered finite element models of structure 3D ($\ell/h = 4$) was performed. Due to accession of mass, the calculated natural frequencies of the covered structure were less than frequencies of corresponding modes of the uncovered structure. Tests on the physical structure indicated that the frequencies were essentially unchanged when backfill was added. The difference between measurements and the computations is apparently due to arching in the sand backfill, which is not properly accounted for in the elastic modal analysis.

Transient analysis of a covered model of structure 3D was performed in which two different backfill wave speeds were assumed in order to investigate their effect on radiation damping. It was found that for the first mode the average radiation damping for the entire structure can be expressed as 15 percent of critical for the softest backfill considered (c_s = 311 fps) and 22 percent for the stiffest backfill (c_s = 622 fps). This is about the same as was found in a previous analysis of an arch, in which damping ranged from 12 to 20 percent of critical. Radiation damping contributes significantly to suppressing resonance in forced vibration tests on the arch; however, resonance in the rectangular structures cannot be attributed to light radiation damping. It appears that another mechanism such as arching, possibly peculiar to the soil type used as backfill for the rectangular structures, plays an important role in allowing resonance to develop under forced vibration.

Nonlinear SDOF models of the rectangular structures were developed and subjected to loading measured during a HEST test on structure 3B. The loading included the HEST cavity pressure and the soil-structure interface pressure. The range of radiation damping ratios obtained during the transient vibration studies were used in the SDOF models to investigate the effect of including damping on the response. The response of the models with 10 percent critical damping were 30 percent to 50 percent less than those of the undamped models. Higher damping appears to be justified by the present calculations and would produce even smaller responses. These findings strongly indicate the need to include

radiation damping in SDOF models of shallow-buried structures in which deflection of the roof results in deflections of the walls and floor. This seems to be the principal mechanism by which energy of vibration is transmitted to the soil and occurs during monotonically increasing deflections of the structure as well as for vibrations.

In order to gain insight into the natural frequencies and damping characteristics of embedded protective structures, the interaction equations for the case of an embedded cylindrical shell were solved. The results are presented in graphical form such that the ratio of embedded in vacuo frequencies and fractions of critical damping can be estimated from knowledge of the in vacuo properties of the cylinder and the properties of the soil. It is shown that these results can be used to interpret the response of structural shapes other than cylinders (in this case, a rectangular structure) providing that the principal mode of deformation is similar (in this case, the ovaling mode).

One remaining uncertainty is whether it is correct to assume a constant fraction of critical viscous damping based on stiffness in the elastic-plastic regime or whether, instead, the damping should vary with displacement. Further research should be aimed at this problem and at developing simple techniques for estimating the radiation damping in a wide range of structural configurations, depths of burial and backfill wave speeds for structures of interest.

REFERENCES

1. Isenberg, J., Levine H. S., and Pang, S. H., "Numerical Simulation of Forced Vibration Tests on a Buried Arch," DNA 4281F, Weidlinger Associates, March 1977.

2. Crowson, R., and Kiger, S., "Vibration Tests and Analyses of ESSEX-V Model Structures," USAEWES report to be published.

3. Wiehle, C. K., and Bockholt, J. L., "Dynamic Analysis of Reinforced Concrete Floor Systems," SRI Project 1219-2 prepared for Defense Civil Preparedness Agency, May 1973.

4. Windham, J. E., and Curtis, J. O., "Effect of Backfill Property and Airblast Variations on the External Loads Delivered to Buried Box Structures," U. S. Army Engineer Waterways Experiment Station, April 1977.

5. Wiehle, C. K., "Evaluation of Existing Structures," Stanford Research Institute Final Report to Civil Defense Preparedness Agency under Contract DAHC 20-71-C-0292, December 1974.

6. Biggs, J. M., "Introduction to Structural Dynamics," McGraw-Hill Book Company, New York, 1964.

7. Baron, M. L., and Parnes, R., "Diffraction of a Pressure Wave by a Cylindrical Shell in an Elastic Medium," 4th U. S. Congress of Applied Mechanics, ASME.

8. Geers, T. L., Presented at the 14th International Congress of Theoretical and Applied Mechanics, Delft, The Netherlands, August-September 1976.

9. Baron, M. L., "The Response of a Cylindrical Shell to a Transverse Shock Wave," 2nd U. S. Congress of Applied Mechanics, ASME, 1955.

10. Mow, C-C, and Pao, Y. H., "The Diffraction of Elastic Waves and Dynamic Stress Concentrations," U. S. Air Force Project Rand Report R-482-PR, April 1971.

APPENDIX I

STUDY OF DISCRETIZATION USED FOR STRUCTURE

The finite element model of the rectangular structure was generated using three-dimensional continuum elements because the walls and roof are too thick to be represented by thin plate elements. A brief study was performed to determine whether the lower deformational modes of the roof slab could adequately be represented by a finite element model having two continuum elements through the thickness or if three or more elements are needed. The geometry of the test problem is shown in Figure I-1. It consists of a 6 feet by 16 feet slab, 11 inches thick, which is simply supported on all sides. By applying appropriate boundary conditions, only one-quarter of the slab needs to be considered.

Normal modes for finite element models of this slab with two and three elements through the thickness were obtained and compared with each other and with anlytic expressions for thin plates. Typical results from the finite element models are shown in Figures I-2 and I-3 where the frequencies of the first and second modes are almost exactly equal to each other. Agreement with measured frequencies, Table I-1, is difficult to evaluate because the roof of the rectangular structure is not simply supported. Agreement with the analytic expression for frequencies of thin plates

$$\omega_{mn} = \pi^2 \left(\frac{M^2}{\ell_L^2} + \frac{N^2}{\ell_S^2} \right) \sqrt{\frac{k}{\mu}} \qquad \text{(I-1)}$$

where

ℓ_L = 16 feet

ℓ_S = 6 feet

k = flexural stiffness, $\frac{Eh^3}{12\ (1-\nu^2)}$

ν = Poisson's Ratio

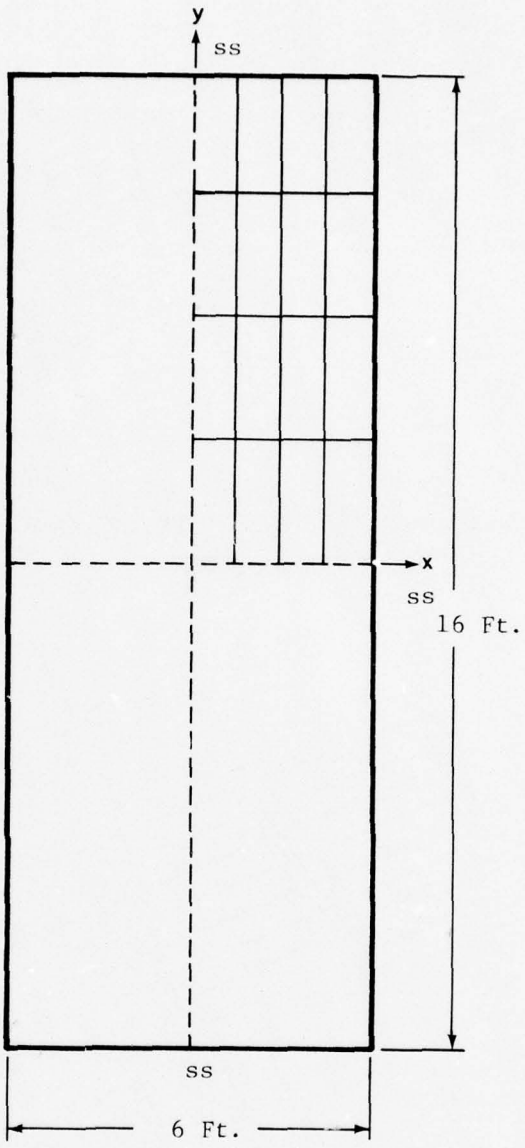
h = thickness of plate

μ = mass per unit area

N = 1; M = 1, 3, 5 for modes 1, 2, 3, respectively

is satisfactory for the first mode, where the finite element model has a slightly lower frequency. This is because the finite element model includes the effects of shear deformation, which increases the flexibility of the system. For the second mode, the finite element model has the higher stiffness. The simplest explanation of this finding is that the finite element model is too stiff to capture the second mode correctly due to discretization error in the X- and Y-directions as well as through the thickness.

The results of this study indicate that the analysis of the rectangular is just as valid with two elements through the thickness of the roof, walls and floor as with three elements. The two element model was therefore adopted on grounds of economy.



ss: simply supported

Thickness: 11 inches

Figure I-1. Geometry of Slab Used to Determine Optimum Discretization for Roof.

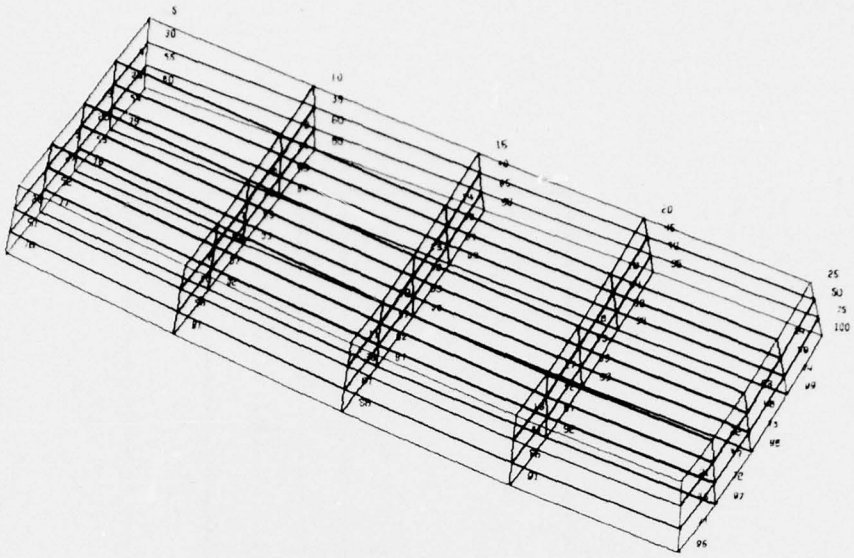


Figure I-2a. Mode 1 of Roof Slab; Three Elements Through Thickness
ω = 146.64 Hz

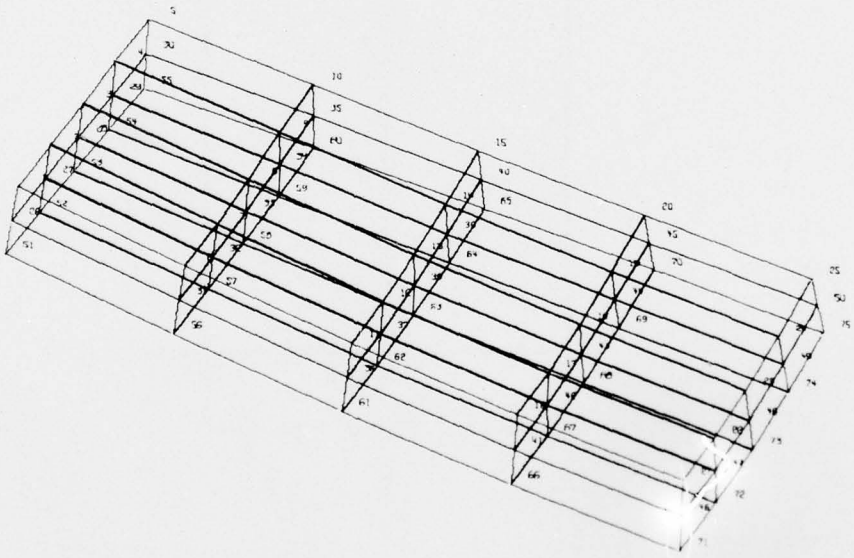


Figure I-2b. Mode 1 of Roof Slab; Two Elements Through Thickness
ω = 146.65 Hz.

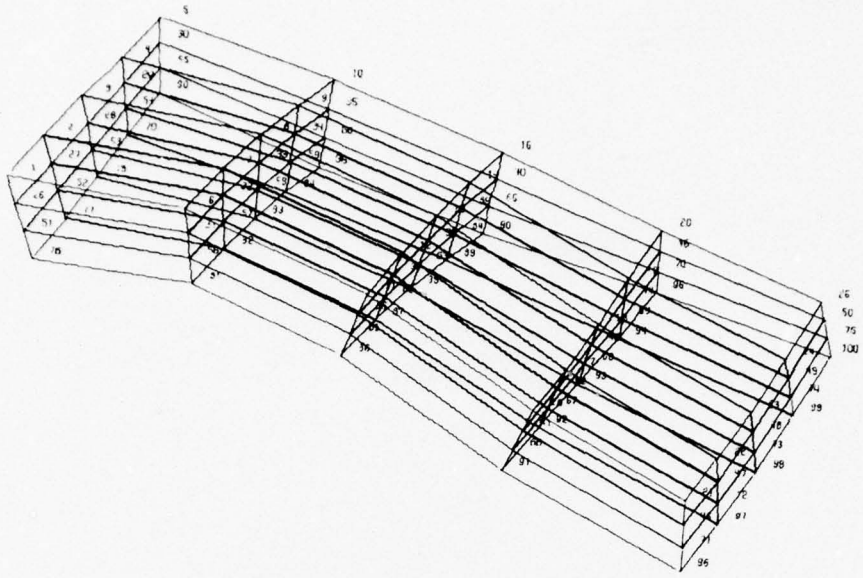


Figure I-3a. Mode 2 of Roof Slab; Three Elements Through Thickness
ω = 267.30 Hz

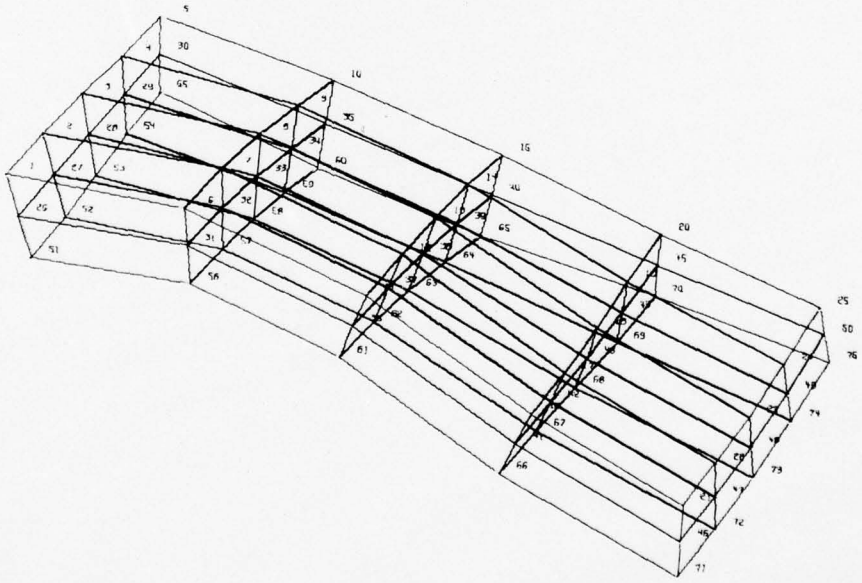


Figure I-3b. Mode 2 of Roof Slab; Two Elements Through Thickness
ω = 267.32 Hz.

TABLE I-1

FREQUENCIES OF ROOF SLAB (Hz)

Mode	Finite Element (Roof Slab)	Analytic (Roof Slab)
1	147	157
2	267	196

Experiment (entire structure) 237 Hz, 415 Hz, 470 Hz, 521 Hz

DISTRIBUTION LIST

DEPARTMENT OF DEFENSE

Assistant to the Secretary of Defense
Atomic Energy
ATTN: Executive Assistant

Defense Advanced Rsch. Proj. Agency
ATTN: TIO
ATTN: NMRO
ATTN: PMO
ATTN: STO

Defense Civil Preparedness Agency
Assistant Director for Research
ATTN: Admin. Officer

Defense Documentation Center
Cameron Station
12 cy ATTN: TC

Defense Intelligence Agency
ATTN: DB-4C, E. O'Farrell
ATTN: DB-4E
ATTN: J. Burfening

Defense Nuclear Agency
ATTN: DDST
2 cy ATTN: SPSS
4 cy ATTN: TITL

Field Command
Defense Nuclear Agency
ATTN: FCTMOF
ATTN: FCPR

Interservice Nuclear Weapons School
ATTN: Document Control

Joint Strat. Tgt. Planning Staff
ATTN: NRI-STINFO Library

Livermore Division, Field Command, DNA
Lawrence Livermore Laboratory
ATTN: FCPRL

NATO School (SHAPE)
ATTN: U.S. Documents Officer

Under Secretary of Def. for Rsch. & Engrg.
ATTN: Strategic & Space Systems (OS)

WWMCCS System Engineering Org.
ATTN: T. Neighbors

DEPARTMENT OF THE ARMY

BMD Advanced Technology Center
Huntsville Office
ATTN: 1CRADABH-X
ATTN: CRDABH-S

Chief of Engineers
ATTN: DAEN-RD
ATTN: DAEN-MCE-D

DEPARTMENT OF THE ARMY (Continued)

Deputy Chief of Staff for Ops. & Plans
ATTN: MOCA-ADL

Deputy Chief of Staff for Rsch. Dev. & Acq.
ATTN: DAMA-AOA-M

Harry Diamond Laboratories
ATTN: DELHD-TI
ATTN: DELHD-NP

Redstone Scientific Information Ctr.
U.S. Army R&D Command
ATTN: Chief, Documents

U.S. Army Ballistic Research Labs.
ATTN: DRXBR-BLE, W. Taylor
ATTN: DRDAR-BLE, J. Keefer
ATTN: DRXBR-X, J. Meszaros
ATTN: Tech. Lib., E. Baicy

U.S. Army Engineer Center
ATTN: ATSEN-SY-L

U.S. Army Engineer Div., Huntsville
ATTN: HNDED-SR

U.S. Army Engineer Div., Ohio River
ATTN: ORDAS-L

U.S. Army Engr. Waterways Exper. Station
ATTN: J. Strange
ATTN: Library
ATTN: W. Flathau
ATTN: R. Walker
ATTN: J. Bolsara

U.S. Army Material & Mechanics Rsch. Ctr.
ATTN: Technical Library

U.S. Army Materiel Dev. & Readiness Cmd.
ATTN: DRXAM-TL

U.S. Army Nuclear & Chemical Agency
ATTN: Library

DEPARTMENT OF THE NAVY

Civil Engineering Laboratory
Naval Construction Battalion Center
ATTN: S. Takahashi
ATTN: Code L08A
ATTN: R. Odello

Naval Electronic Systems Command
ATTN: PME 117-21A

Naval Facilities Engineering Command
ATTN: Code 04B
ATTN: Code 09M22C
ATTN: Code 03A

Naval Material Command
ATTN: MAT 0323

DEPARTMENT OF THE NAVY (Continued)

Naval Postgraduate School
ATTN: Code 2124, Tech. Rpts. Librarian

Naval Research Laboratory
ATTN: Code 2627

Naval Surface Weapons Center
ATTN: Code F31

Naval Surface Weapons Center
Dahlgren Laboratory
ATTN: Tech. Library & Info. Services Branch

Naval Underwater Systems Center
ATTN: Code EM, J. Kalinowski

Naval War College
ATTN: Code E11

Naval Weapons Evaluation Facility
ATTN: Code 10

Office of Naval Research
ATTN: Code 474, N. Perrone
ATTN: Code 715
ATTN: Code 461, J. Warner

Office of the Chief of Naval Operations
ATTN: Op-981
ATTN: Op-03EG

Director
Strategic Systems Project Office
ATTN: NSP-43

DEPARTMENT OF THE AIR FORCE

Air Force Geophysics Laboratory
ATTN: LWW, K. Thompson
ATTN: SUOL

Air Force Institute of Technology, Air University
ATTN: Library, AFIT Bldg. 640, Area B

Air Force Systems Command
ATTN: DLCAW

Air Force Weapons Laboratory
ATTN: DES-S, M. Plamondon
ATTN: SUL

Assistant Chief of Staff
Intelligence
ATTN: INATA

Deputy Chief of Staff
Research, Development, & Acq.
ATTN: AFRDQSM

Deputy Chief of Staff
Programs & Resources
ATTN: PRE

Foreign Technology Division, AFSC
ATTN: NICD Library

Rome Air Development Center, AFSC
ATTN: Documents Library/TSLD

DEPARTMENT OF THE AIR FORCE (Continued)

Space & Missile Systems Organization/MN
ATTN: MNN

Strategic Air Command/XPFS
ATTN: NRI-STINFO Library

DEPARTMENT OF ENERGY

Department of Energy
Albuquerque Operations Office
ATTN: Doc. Con. for Tech. Library

Department of Energy
Library Room G-042
ATTN: Doc. Con. for Classified Library

Department of Energy
Nevada Operations Office
ATTN: Doc. Con. for Tech. Lib.

University of California
Lawrence Livermore Laboratory
ATTN: Doc. Con. for L-96, L. Woodruff
ATTN: Doc. Con. for Technical Information
Department Library

Los Alamos Scientific Laboratory
ATTN: Doc. Con. for Reports Library
ATTN: Doc. Con. for R. Bridwell

Sandia Laboratories
Livermore Laboratory
ATTN: Doc. Con. for Library & Security
Classification Division

Sandia Laboratories
ATTN: Doc. Con. for 3141
ATTN: Doc. Con. for A. Chabai
ATTN: Doc. Con. for L. Hill

OTHER GOVERNMENT AGENCIES

Central Intelligence Agency
ATTN: RD/SI, Rm. 5G48, Hq. Bldg. for
J. Ingley

Department of the Interior
Bureau of Mines
ATTN: Tech. Library

DEPARTMENT OF DEFENSE CONTRACTORS

Aerospace Corporation
ATTN: Tech. Info. Services

Agbabian Associates
ATTN: M. Agbabian

Applied Theory, Inc.
2 cy ATTN: J. Trulio

Avco Research & Systems Group
ATTN: Library, A830

Battelle Memorial Institute
ATTN: Library

BDM Corporation
ATTN: Corporate Library

DEPARTMENT OF DEFENSE CONTRACTORS (Continued)

Boeing Company
ATTN: Aerospace Library

California Research & Technology, Inc.
ATTN: Library
ATTN: S. Shuster
ATTN: K. Kreyenhagen

Calspan Corporation
ATTN: Library

Civil/Nuclear Systems Corporation
ATTN: J. Bratton

University of Dayton
Industrial Security Super, KL-505
ATTN: H. Swift

EG&G Washington Analytical Services Center, Inc.
ATTN: Library

Eric H. Wang
Civil Engineering Rsch. Fac.
ATTN: N. Baum

Gard, Inc.
ATTN: G. Neidhardt

General Electric Co.-TEMPO
Center for Advanced Studies
ATTN: DASIAC

IIT Research Institute
ATTN: M. Johnson
ATTN: R. Welch
ATTN: DOcuments Library

Institute for Defense Analyses
ATTN: Classified Library

Kaman AviDyne
Division of Kaman Sciences Corporation
ATTN: E. Criscione
ATTN: N. Hobbs
ATTN: Library

Kaman Sciences Corporation
ATTN: Library

Lockheed Missiles & Space Co., Inc.
ATTN: T. Geers
ATTN: Tech. Info. Ctr., D/Coll.

McDonnell Douglas Corporation
ATTN: R. Halprin

Merritt CASES, Inc.
ATTN: J. Merritt
ATTN: Library

Nathan M. Newmark
Consulting Services
ATTN: N. Newmark

DEPARTMENT OF DEFENSE CONTRACTORS (Continued)

Physics International Co.
ATTN: E. Moore
ATTN: D. Orphal
ATTN: R. Swift
ATTN: Doc. Con. for Technical Library
ATTN: L. Behrmann
ATTN: F. Sauer

R&D Associates
ATTN: R. Port
ATTN: A. Latter
ATTN: H. Brode
ATTN: J. Lewis
ATTN: Technical Information Center

R&D Associates
ATTN: H. Cooper

Science Applications, Inc.
ATTN: Technical Library

Science Applications, Inc.
ATTN: D. Bernstein
ATTN: D. Maxwell

Southwest Research Institute
ATTN: W. Baker

SRI International
ATTN: G. Abrahamson

Systems, Science & Software, Inc.
ATTN: T. Cherry
ATTN: Library
2 cy ATTN: D. Grine//T. Riney

TRW Defense & Space Sys. Grp.
ATTN: Technical Information Center
ATTN: P. Dai

TRW Defense & Space Sys. Grp.
ATTN: E. Wong

Weidlinger Assoc., Consulting Engineers
ATTN: M. Baron

Weidlinger Assoc., Consulting Engineers
ATTN: G. Wojcik
2 cy ATTN: J. Isenberg

Westinghouse Electric Corp.
Marine Division
ATTN: W. Volz